공학박사학위논문

Computational Study on Active Flow Control using Synthetic Jet for Three-dimensional Aircraft Configuration

Synthetic jet 을 이용한 3 차원 날개 능동 유동제어에 관한 수치적 연구

2014 년 8 월

서울대학교 대학원
협동과정 계산과학전공
김 민 희

Computational Study on
Active Flow Control using Synthetic Jet for
Three-dimensional Aircraft Configuration

Synthetic jet 을 이용한
3차원 날개 능동 유동제어에 관한 수치적 연구

지도교수 김 종 암

이 논문을 공학박사학위 논문으로 제출함
2014 년 6 월

서울대학교 대학원
협동과정 계산과학전공
김 민 희

김민희의 공학박사학위 논문을 인준함
2014 년 6 월

위 원 장 : 姜 明 圓

부위원장 : 金 鍾 岩

위   원 : 鄭 仁 碩

위   원 : 金 奎 弘

위   원 : 下 喆 燮

Abstract

The present study deals with flow characteristics of synthetic jets for efficient flow control performance. It consists of two parts: flow characteristics of synthetic jets depending on exit configuration and flow control using synthetic jets over Blended Wing Body (BWB) configuration.

In first part, flow characteristics of synthetic jets have been computationally investigated for different exit configurations under a cross flow condition. The exit configuration of a synthetic jet substantially affects the process of vortex generation and evolution, which eventually determines the mechanism of jet momentum transport. Two types of exit configurations were considered: one is a conventional rectangular exit, and the other is a series of circular holes. The interactions of synthetic jets with a freestream were performed by analyzing the vortical structure characteristics. The effectiveness of flow control was evaluated by examining the behavior of the wall shear stress. It was observed that the circular exit provides better performance than the rectangular exit in terms of sustainable vortical structure and flow control capability. According to a hole gap and a hole diameter of circular exit, comparative studies were then conducted with all the other parameters fixed. Detailed computations reveal that the hole gap yields a much more significant effect on flow characteristics than the hole diameter, which turned out to be relatively minor. Based on the strength and the persistency of jet vortices, the circular exit with a suitable hole gap formed critical jet vortices that beneficially affected separation control. This

indicates that the flow control performance of circular exit array could be remarkably improved by applying a suitable dimensionless hole parameter.

Based on the results of exit configuration, the second part deals with flow control strategy over BWB configuration. Flow structures were examined by analyzing the baseline characteristics of BWB configuration when synthetic jet was off. Based on the aerodynamic data and flow structure, a strategy for flow separation control on BWB configuration was established. Based on the aerodynamic data and flow structure, synthetic jet actuators were installed to prevent leading-edge stall at a relatively high angles of attack. All-actuators-on case and selective-actuators-on case were examined to find effective flow control method. Two types of exit locations are considered for analyzing flow mechanism: one is outboard array jets, and the other is inboard array jets. The interactions of synthetic jets with a free stream were performed by analyzing the vortical structure and the surface pressure characteristics. The effectiveness of flow control was evaluated by examining the aerodynamic coefficient and flow structures. As a result, the vortex breakdown point is moved toward the outboard section by synthetic jets, and the separation flow shows a stable structure. Based on the flow structure in overall speed rage, flow control strategy of low speed flight is applied to flow control of high speed flight. This shows effective flow control strategy applicable to all speed flight.

Through numerical analyses on flow characteristics of synthetic jets, it is observed that the synthetic jets under suitable actuating conditions beneficially change the local flow feature and vortex structure to bring a significant improvement of the wing aerodynamics acting on the three-dimensional aircraft configuration in the stall angle.

Table of Contents

List of Tables

List of Figures

Chapter I
Introduction

1.1 Literature Review

1.1.1 Synthetic Jet

Synthetic jets have been widely used for flow control [1,2], jet mixing enhancement [3], and heat transfer [4]. In particular, control of flow separation by means of synthetic jets is known to be quite effective in a variety of flow conditions [5]. A typical synthetic jet actuator consists of a small cavity with an oscillating diaphragm at its bottom side and an orifice plate at the opposite side, as shown in Fig. 1.1. As the result of the alternating of suction and blowing produced by the movement of diaphragm, a succession of vortex fairs is produced and propagates away from the orifice. The vortex formation process has significance with regards to performance of flow control devices. Studies on synthetic jets have focused on the formation of a synthetic jet in a turbulent mixing layer, and assessed its behavior under various conditions.

Many researchers and engineers produced experimental results in jet characteristics and jet vortex formation. Crook and Wood examined the behavior of synthetic jets under a quiescent condition, a cross-flow, and a

boundary layer [6]. They studied the delay of flow separation on a circular cylinder by using hotwire anemometry and flow visualization techniques. Wang *et al.* investigated flow separation control of a circular cylinder using a synthetic jet positioned at the front stagnation point by the particle image velocimetry (PIV) technique [7]. They also modified the wake behind a circular cylinder by a synthetic jet and analyzed the vortex shedding modes and mechanism [8]. Amitay and Cannelle studied the evolution and transient behavior of finite span synthetic jets using hot wire anemometry and PIV techniques. They examined the effect of the slot aspect ratio on the development of the synthetic jet, and the spatial evolution of secondary three-dimensional vortical structures in the flow field [9,10].

At the same time, a number of numerical studies have also been carried out. Mittal *et al.* examined the formation and evolution of a synthetic jet and compared the dynamical characteristics in quiescent and cross-flow conditions [11]. Rumsey *et al.* performed a study of synthetic jet flows into a turbulent boundary layer crossflow through a circular orifice [12]. W. Nitsche *et al.* studied flap separation control by periodic excitation near the flap for high-lift configuration [13,14]. Kim and Kim numerically investigated the frequency-dependent flow control mechanisms of synthetic jets on an airfoil, and proposed multi-location synthetic jets to mitigate the unstable flow structures of a high-frequency jet [15]. Subsequently, Kim *et al.* applied synthetic jets to improve the aerodynamic performance of tilt-rotor UAV airfoils in hovering and transition flight modes [16]. Zhong *et al.* examined the vortex structures produced by a synthetic jet in water, and

presented the vortex roll-up criterion according to the Stokes length using experimental and numerical methods [17]. In addition, the fluid physics underlying the interaction process between circular synthetic jet and a laminar boundary layer was investigated by 3-D numerical simulations.

1.1.2 Piezoelectirically-driven Synthetic Jet

A synthetic jet actuator is driven by a voice-coil motor, a piezoelectric diaphragm or a piston in a periodic manner with zero net mass-flux [18,19]. Example applications have shown that many types of synthetic jet can control the separated-region include airfoil and bluff bodies [20,21]. Figure 1.2 shows several drive types of piezoelectric component, which can be applied to a practical synthetic jet actuator. The oscillating diaphragm used in the synthetic jet cavity is usually driven by using electrical or mechanical power. When driven with AC (Alternating Current) signal, piezoelectric disks oscillate in the same manner as a piston or a shaker, and they also require the reduced number of moving parts which are prone to failure [22]. Because of these advantages, several investigators have adopted piezoelectric disks in synthetic jets to attempt to make the systems lighter, increase efficiency and save resource [24,25]. Although, these piezoelectric disks have been successful in generating high velocities capable of altering the flow fields, the devices operate at high frequencies, consequently requiring high amounts of power. In this study, piezoelectric diaphragm is used as active membrane in the jet cavity. These composites have the ability

to produce micro scale displacement and provide a wide bandwidth response as well as being lightweight. Such advantages make them suitable for flow control purposes, as demonstrated by Mossi *et al.* [25-27].

1.1.3   Lambda Wing Aerodynamics

Lambda wing platforms have been the subject of experimental investigation by Australia, Canada, UK and US over more than a decade. They studied the development of wing flows and their subsequent impact on flight mechanics for lambda wing configurations [28]. The fundamental geometric features of pure edge-aligned or near-lambda wings are the presence of a concave trailing edge crank at or near mid-semispan, and a convex trailing edge crank outboard, closer to a pointed wing tip. These allow lambda wings to combine increased aspect ratio and taper with platform edge alignment, relative to a single-panel swept-tapered wing. The introduction of cranks presents some problems for the aerodynamic performance of these wings.

The introduction of a local minimum in chord associated with the inboard trailing edge crank results in a local maximum in section lift coefficient at the inboard crank. Conversely, the outboard crank generates a local minimum in local lift coefficient. A second local maximum in lift coefficient occurs between the local minimum at the outboard crank and the tip, where loading goes to zero. Hence peak local lift coefficient on lambda wings will occur either near the inboard crank or slightly inboard of the

pointed wing tip. The onset of flow separation can be assumed to happen at or near either of these local maxima in lift coefficient. At low speeds, assuming low levels of camber, the tendency will be towards flow separation caused by the adverse pressure gradient downstream of the leading edge suction peak. At transonic Mach numbers, the local loading at the inboard crank will tend to be exacerbated by the unsweeping of isobars locally across the crank, increasing the tendency towards shock induced flow separation at this location. These flow separation mechanisms have been observed on a range of lambda wing platform tests performed during the 1990s.

A consequence of the onset of flow separation near the inboard crank is the rapid outboard spread of the flow separation from the onset location, producing fully separated flow over the outboard wing panel and any trailing edge devices installed there. This has significant implications for the flight mechanics and controllability of lambda wing configurations in general and flying lambda wing configurations in particular. For the latter, lack of auxiliary control surfaces and short moment arm for trailing edge devices imply a relative lack of available control power in pitch. The loss of effectiveness of outboard control surfaces also implies reduced lateral control authority.

1.1.4   Flow Separation on Lambda Wing Flight Mechanics

The natural consequence of the onset and development of flow separation over the outer portion of the lambda wing is that the centroid of

lift of the wing will tend to shift inboard and forward, resulting in change of static margin, or pitch-up [28]. Pitch-up is the usual consequence of combining high sweep and aspect ratio for aft-swept wings, with the boundaries and palliatives for this behavior being the subject of much study in the 1940s and 1950s [29]. It appears that lambda wings are inherently more susceptible to large, rapid, unstable pitch breaks than simple swept tapered wings of the same sweep and aspect ratio. The US Air Force Research Laboratory (AFRL) and UK Defense Research Agency (DRA) conducted tests of a simple 40° edge-aligned lambda wing and identified serious shortcomings in both lift curve slope and maximum useable lift relative to conventional swept-tapered wings of similar leading edge sweep and aspect ratio [30].

Given a fixed wing platform, the usual means of addressing the issue of pitch-up at low speeds, as indicated by Ref. 29, is to delay flow separation by weakening the adverse pressure gradients downstream of the leading edge using camber, either through simple droop or the introduction of a wing leading edge device. The tests described in Ref. 30 included a variety of leading edge flap settings, which had a limited impact on the pitch-up problem. Subsequently much of the further experimental investigations into the characteristics of the pure lambda wing involved high Reynolds number testing of half-models with high-lift systems for low speed launch and recovery, and for transonic maneuver. The bulk of the high Reynolds number testing for lambda wings involved US-manufactured models being tested in UK tunnels. Unlike the earlier tests, these involved aerodynamically

designed wings with representative levels of twist and camber. Transonic tests at high Reynolds number [31] indicated that the pitch-up problem persisted at likely conditions for high-subsonic maneuver, although the flow separation mechanism for these wings was shock induced, rather than related to leading edge separation.

1.1.5 1303 UCAV Configuration

Unmanned combat air vehicles (UCAVs) possessing lambda wing platforms continue to be of interest to the international aerospace community from both an experimental and computational perspective. Their three-dimensional configuration can give rise to complex flow patterns, whereby the occurrence of separation and stall can vary substantially along the span. Flow separation, transition from laminar to turbulent flow, and nonlinear vortex dynamics such as vortex interactions and breakdown are examples of the types of flow features that may be encountered when considering such geometries.

In recent years, the 1303 UCAV configuration, developed by the U.S. Air Force Research Laboratory in conjunction with The Boeing Company [32], has been examined using both experimental and computational techniques, as shown in Fig. 1.3. Experimentally, wind-tunnel investigations at moderate Reynolds numbers have been performed by Bruce [33] and McParlin *et al.* [34] using a variety of leading edge geometries, as well as by Ghee [35] and Ghee and Hall [36]. Ol [37] characterized the sectional flow

structure at lower Reynolds numbers in terms of patterns of mean velocity and Reynolds stress using particle image velocimetry (PIV) in a water channel facility. Dye visualization of the processes of flow separation and vortex formation were addressed in a water facility by Nelson *et al.* [38]. Kosoglu [39] employed dye visualization to qualitatively describe the three-dimensionality, in conjunction with PIV, with emphasis on the flow structure in planes that were oriented parallel to the wing surface. This geometry has also been studied computationally by a wide range of researchers as part of The Technical Cooperation Program under the auspices of the Aerospace Systems Group's Technical Panel 5 (AER TP-5) using both low-order structured [40-42]. The general conclusion drawn from these works was that the computational fluid dynamics coupled with an appropriate turbulence model was effective at predicting the magnitudes of lift and drag forces at the lower angles of attack where the flow remains primarily attached, but was unable to maintain this performance at the higher angles where separation becomes more widespread.

For some UCAV applications, limits on useable lift may be acceptable assuming no demanding requirements for maneuver in up-and-away conditions, however, limiting useable lift has a much more significant impact on air vehicle performance at launch and recovery phases of the mission. Low useable maximum lift coefficient implies high landing and take-off speeds, and hence becomes a configuration size driver, an issue for all potential UCAVs, but particularly for those with aspirations towards carrier-based operations. Therefore, the onset of flow separation from the

leading edge of lambda wing UCAVs is a driving factor in their cost and size, and their suitability for operations from aircraft carriers.

Technologies that broaden the roles and capabilities of UCAV are of significant interest to the aerospace community. This is due to a sharp rise in the demand and applications for UCAV for both military and civilian operations. Active flow control is one such technology that holds considerable promise in advancing the aerodynamic performance and maneuvering of UCAV. The technology is based on the use of small-scale actuators that elicit desired changes in the flow state by altering the balance of flowfield energy using flow-manipulation methods. Patel *et al.* [43] studied the use of dielectric barrier discharge plasma actuators for hingeless flow control over a 47 ° 1303 UCAV. They implemented at the wing leading edge to provide longitudinal control without the use of hinged control surfaces. Amitay [44] experimentally investigated the application of leading edge separation control on an UAV with 50 ° leading edge in a full-scale close-return wind tunnel using arrays of synthetic jet actuators. A numerical analysis of 1303 UCAV with and without simple deployable vortex flaps was also conducted to understand the flowfield environment around the vehicle [45,46]. Cung *et al.* [47] examined the critical design for the 1303 UCAV to provide increased fidelity for the aerodynamic analysis required for a carrier landing suitability. In addition, an optimization study has been conducted attempting to minimize drag in the cruise configuration subject to constraints designed to avoid flow separation at take-off [48].

1.2   Objectives and Contributions

The objective of this dissertation is to study flow characteristics of synthetic jets for efficient flow control performance to bring an improvement of the wing aerodynamics acting on Blended Wing Body (BWB) configuration, which is modified from 1303 UCAV. It consists of two parts: flow characteristics of synthetic jets depending on exit configuration and flow control strategy over BWB configuration.

- Flow Characteristics of Synthetic Jets

The focus of the first part is to investigate the local flow feature and vortex structure, and analyze wall shear stress distributions in terms of flow control effect. In order to achieve the goal, the flow characteristics of a conventional rectangular slot and a multiple serial circular exit are firstly investigated. Based on the observed flow features, comparative studies of the circular exit are then conducted with variations of a hole gap and a hole diameter. Finally, by comparing the results of the flow characteristics, most effective exit configuration is obtained when other flow control parameters are identical.

- Flow Control of Wing

Based on the results of exit configuration, the second part deals with flow control strategy over BWB configuration. Experimental and numerical data are examined by analyzing the baseline characteristics of BWB

configuration when synthetic jet is off. Based on the aerodynamic data and flow structure, synthetic jet actuators are installed to prevent leading edge stall at high angles of attack. Selective-actuators-on case is examined to find effective flow control method. Two types of exit locations are considered for analyzing flow mechanism: one is inboard array jets, and the other is outboard array jets. Flow control strategy of low speed flight is also applied to flow control of high speed flight. By comparing the results of the flow control characteristics, flow control strategy at high angle of attack is established over BWB configuration in overall flight condition.

1.3   Organization of Thesis

The dissertation is organized as follows. In Chapter Ⅱ, a brief description of the governing equations are given. In Chapter Ⅲ, flow characteristics of synthetic jets depending on the exit configuration are described. Then, baseline flowfield structure and flow control strategy over BWB configuration are analyzed in Chapter Ⅳ. Finally, conclusions are drawn in Chapter Ⅴ.

Chapter II
Numerical Approaches

2.1 Governing Equations

The governing equations for compressible viscous fluid motion are given in a conservative form using Cartesian-tensor notation of

$$\frac{d\rho}{dt} + \frac{\partial}{\partial x_k}(\rho u_k) = 0 \tag{2.1}$$

$$\frac{\partial(\rho u_i)}{\partial t} + \frac{\partial}{\partial x_j}(\rho u_i u_j) = -\frac{\partial p}{\partial x_i} + \frac{\partial}{\partial x_j}\left\{\mu\left(\frac{\partial u_i}{\partial x_j} + \frac{\partial u_j}{\partial x_i} - \frac{2}{3}\delta_{ij}\frac{\partial u_k}{\partial x_k}\right)\right\} \tag{2.2}$$

where ρ is the density, u_i is the velocity component in x_i coordinate direction, p is the pressure, and μ is the absolute viscosity. Equation (2.1) and (2.2) are the equation of mass conservation and the equation of momentum conservation, respectively. It is necessary to include the equation of energy conservation along with the equation of state to give a complete equation does not need to be solved for incompressible flow problems unless the heat transfer on the boundaries and the temperature distribution in the flowfield are a matter of concern.

If the density of the flow is constant, equation (2.1) can be reduced to

$$\frac{\partial u_k}{\partial x_k} = 0 \qquad\qquad (2.3)$$

and dividing equation (2.2) by density ρ results in

$$\frac{\partial u_i}{\partial t} + \frac{\partial}{\partial x_j}\left(u_i u_j\right) = -\frac{\partial p}{\partial x_i} + \frac{\partial}{\partial x_j}\left\{\nu\left(\frac{\partial u_i}{\partial x_j} + \frac{\partial u_j}{\partial x_i} - \frac{2}{3}\delta_{ij}\frac{\partial u_k}{\partial x_k}\right)\right\} \qquad (2.4)$$

where ν is the kinematic viscosity and the pressure p absorbs the density, i.e., $p = p/\rho$. The divergence of velocity is zero from equation (2.3), but it is left in equation (2.4) on purpose because the velocity field is not divergence free until the solution is converged. When the divergence free condition is applied and ν is assumed to be constant for laminar flow calculations, equation (2.4) is then reduced to

$$\frac{\partial u_i}{\partial t} + \frac{\partial}{\partial x_j}\left(u_i u_j\right) = -\frac{\partial p}{\partial x_i} + \nu\frac{\partial^2 u_i}{\partial x_j \partial x_j} \qquad\qquad (2.5)$$

It should be noted that equation (2.3) and (2.4) give a complete description of the motion of an incompressible fluid. Thus, the equation of energy conservation will be solved only when necessary.

13

2.2 Turbulence Models

For an adequate description of turbulent flow field within the framework of a Reynolds Averaged Navier-Stokes (RANS) formulation, Menter's standard k-ω model Shear Stress Transport (SST) model [51], Menter's k-ω SST developed in 2003 [52], and DES (Detached Eddy Simulation) based on k-ω SST model [52,53] are employed. These turbulence models are composed of two transport equations of the turbulent kinetic energy k and the dissipate rate ω.

2.2.1 The Standard Menter's k-ω SST Model

The k-ω model [49] performs well and is superior to the k-ε model [50] within the laminar sublayer. However, the k-ω model has been shown to be influenced strongly by specification of freestream value of ω outside the boundary layer. There, the k-ω model does not appear to be an ideal model for applications in the wake region of the boundary layer. On the other hand, the k-ε model behaves superior to that of the k-ω model in the outer portion and wake regions of the boundary layer, but inferior in the inner region of the boundary layer. To include the best features of each model, Menter has combined different elements of the k-ε and k-ω models to form a new two-equation model. This model incorporates the k-ω model for the inner region of the boundary layer, and it switches to the k-ε model for the outer and wake region of the boundary layer.

The original k-ω model is multiplied by a function F_1 and the transformed k-ε model by a function (1-F_1). The blending function F_1 is set to be one in the near wall region and zero far away from the wall surface. Both the models are combined as:

$$\frac{\partial \rho k}{\partial t} + \frac{\partial}{\partial x_j}\left(\rho k u_j\right) = \tau_{ij}\frac{\partial u_i}{\partial x_j} - \beta^* \rho \omega k + \frac{\partial}{\partial x_j}\left[\left(\mu + \sigma_k \mu_t\right)\frac{\partial k}{\partial x_j}\right]$$

$$\frac{\partial \rho \omega}{\partial t} + \frac{\partial}{\partial x_j}\left(\rho \omega u_j\right) = \frac{\gamma}{\nu_T}\tau_{ij}\frac{\partial u_i}{\partial x_j} - \beta \rho \omega^2 + \frac{\partial}{\partial x_j}\left[\left(\mu + \sigma_\omega \mu_t\right)\frac{\partial \omega}{\partial x_j}\right] \qquad (2.5)$$

$$+ 2\left(1 - F_1\right)\rho \sigma_{\omega_2}\frac{1}{\omega}\frac{\partial k}{\partial x_j}\frac{\partial \omega}{\partial x_j}$$

The constant appearing in Eq. (2.5) are evaluated in the following relation by using the blending function;

$$\Phi = F_1\Phi_1 + \left(1 - F_1\right)\Phi_2 \qquad (2.6)$$

where Φ_1 represents the constants associated with the $k - \omega$ model (when $F_1 = 1$), and Φ_2 represents the constants associated with the $k - \varepsilon$ model (when $F_1 = 0$) and the constants for Φ are specified as follows;

$$\gamma_1 = \beta_1 / \beta^* - \sigma_{\omega 1}\kappa^2 / \sqrt{\beta^*}, \quad \gamma_2 = \beta_2 / \beta^* - \sigma_{\omega 2}\kappa^2 / \sqrt{\beta^*}$$

$$\sigma_{k1} = 0.85, \quad \sigma_{k2} = 1.0, \quad \sigma_{\omega 1} = 0.5, \quad \sigma_{\omega 1} = 0.856$$

$$\beta^* = 0.09, \quad \beta_1 = 0.075, \quad \beta_1 = 0.0828, \quad \kappa = 0.41$$

In addition, F_1 is a switching function from the $k-\omega$ model to the $k-\varepsilon$ model based on the distance from the nearest solid surface and defined as follows ;

$$F_1 = \tanh\left[\min\left(\max\left(\frac{\sqrt{k}}{\beta^*\omega y}, \frac{500\nu}{y^2\omega}\right), \frac{4\rho\sigma_{\omega_2}k}{CD_{k\omega}y^2}\right)\right]^4 \qquad (2.7)$$

where y is the distance to the nearest surface and CD_{kw} is the positive portion of the cross-diffusion term

$$CD_{k\omega} = \max\left[2\rho\sigma_{\omega_2}\frac{1}{\omega}\frac{\partial k}{\partial x_j}\frac{\partial\omega}{\partial x_j}, 10^{-20}\right] \qquad (2.8)$$

The eddy viscosity is defined to limit the turbulent shear stress as

$$\mu_t = \frac{0.31\rho k}{\max\left[0.31\omega, \Omega F_2\right]} \qquad (2.9)$$

where is Ω is the absolute value of the vorticity and F_2 is included to prevent singular behavior in the freestream where Ω goes to zero and given by:

$$F_2 = \tanh\left[\max\left(\frac{\sqrt{k}}{\beta^*\omega y}, \frac{500\nu}{y^2\omega}\right)\right]^2 \qquad (2.10)$$

Note that it is generally recommended to employ the production limiter, which replaces the term of P in the k-equation by:

$$P = \tau_{ij}\frac{\partial u_i}{\partial x_j} = \min(P, 20\beta^*\omega k) \qquad (2.11)$$

The boundary conditions and freestream values are given as follows:

$$\frac{U_\infty^2}{10^5\,\mathrm{Re}_L} < k_{farfield} < \frac{U_\infty^2}{10\,\mathrm{Re}_L}$$
$$\frac{U_\infty}{L_{farfield}} < \omega_{farfield} < \frac{10U_\infty}{L_{farfield}}$$
$$k_{wall} = 0 \qquad (2.12)$$
$$\omega_{wall} = \frac{60\nu}{\beta_1(\triangle d)^2}$$

The $L_{farfield}$ is the approximate length of the computational farfield domain from the wall, and a freestream turbulent viscosity μ_t has a value between 10^{-5} and 10^{-2} times the freestream laminar viscosity. The $\triangle d$ is the distance of the first point away from the wall.

2.2.2 The k-ω SST Model (Menter *et al.*, 2003)

The k-ω SST-2003 has several relatively minor variation from the original SST developed in 1994. The model enhancements cover a modified near wall treatment of the equations, which allows a more flexible grid forms. This advantage reduces the problem of grid induced separation for industrial flow simulations. The changes are in the definition of eddy viscosity and in the production limiter. The magnitude of vorticity in the eddy viscosity is changed to the strain invariant (S) in its definition as follows:

$$\mu_t = \frac{0.31\rho k}{\max\left[0.31\omega, SF_2\right]} \qquad (2.13)$$

where $S = \sqrt{2S_{ij}S_{ij}}$

The limiting constant and the second term of $CD_{k\omega}$ is also changed as follows:

$$P = \min(P, 10\beta^* \omega k)$$

$$CD_{k\omega} = \max\left[2\rho\sigma_{\omega_2}\frac{1}{\omega}\frac{\partial k}{\partial x_j}\frac{\partial \omega}{\partial x_j}, 10^{-10}\right] \qquad (2.14)$$

The changed coefficients are $\gamma_1 = 5/9$, $\gamma_2 = 0.44$.

2.2.3   SST-DES Model (Strelets *et al.*, 2001)

Detached Eddy Simulation (DES) is a hybrid turbulence model developed by Spalart and associates (Spalart *et al.*, 1997). Although the DES formulation is immediate only on the basis of the S-A or other models which use a distance to the wall as a turbulence length scale, the DES/S-A link is not fundamental, and other models can be built into DES. The idea behind the DES model of Strelets *et al.* (2001) is to switch from the standard SST-RANS model to an LES model in those regions where the turbulent length, predicted by the RANS model is larger than the local grid spacing. In this case, the length scale used in the computation of the dissipation rate in the equation for the turbulent kinetic energy is replaced by the local grid spacing.

The length scale of this model in terms of k and ω reads as

$$l_{k-\omega} = k^{1/2} / (\beta^* \omega) \tag{2.15}$$

This length scale should be replaced in with the DES length scale

$$\tilde{l} = \min(l_{k-\omega}, C_{DES}\Delta) \tag{2.16}$$

In SST-DES formulation, dissipative term of the *k*-transport equation is expressed as DES length scale.

19

$$D_{RANS}^{k} = \rho \beta^{*} k \omega = \rho k^{3/2} / l_{k-w}$$
$$D_{DES}^{k} = \rho k^{3/2} / \tilde{l}$$
$$(2.117)$$

Eq. (2.21) can now be rewritten as

$$D_{RANS}^{k} = \rho \beta^{*} k \omega$$
$$D_{DES}^{k} = \rho \beta^{*} k \omega F_{DES}$$
$$(2.18)$$

where

$$F_{DES} = \max\left(\frac{l_{k-w}}{C_{DES}\Delta}, 1\right)$$

The grid spacing $\triangle$ is the maximum local grid spacing ($\triangle$ =max($\triangle$x, $\triangle$y, $\triangle$z)) in case of a Cartesian grid, β^* is a constant of the SST model. Just like the classical, RANS, DES formulation has two branches, k-ω model and k-ε model. Although in the major part of the region where DES functions in LES mode only the k-ε model is important, since precisely this branch is active there, we still have performed separate calibrations of the C_{DES} constants for the two branches and then blended the values obtained with the use of Menter's blending function F_1 (Menter, 1993):

20

$$C_{DES} = (1 - F_1)C_{DES}^{k-\varepsilon} + F_1 C_{DES}^{k-\omega} \qquad (2.19)$$

where $C_{DES}^{k-\varepsilon} = 0.61$, $C_{DES}^{k-\omega} = 0.78$ from the numerical experiments about isotropic turbulence.

2.2.4 Zonal SST-DES Model (Menter *et al.*, 2003)

The main practical problem with the DES formulation is that there is no mechanism of preventing the limiter of becoming active in the attached portion of the boundary layer. This will happen when the local surface grid spacing $\triangle_s$ is less to the boundary layer thickness $\triangle_s < c\,\delta$ with c of the order of one.

For fine grids, the switch from RANS to DES can take place somewhere inside the boundary layer and produce a premature (grid-induced) separation. In order to reduce the grid influence of the DES-limiter on the RANS part of the boundary layer, the SST model offers the option to protect the boundary layer from the limiter. This is achieved again with the help of the zonal formulation underlying the SST model. The following modification significantly reduces the influence of the DES limiter on the boundary layer portion of the flow:

$$
\begin{aligned}
D_{RANS}^{k} &= \rho \beta^* k \omega \\
D_{M-DES}^{k} &= \rho \beta^* k \omega F_{M-DES}
\end{aligned}
\qquad (2.20)
$$

where

$$F_{M-DES} = \max\left(\frac{l_{k-w}}{C_{DES}\Delta}(1 - F_{sst}), 1 \right) \quad with \quad F_{sst} = 0, F_1, F_2$$

In this equation, F_{SST} can be selected from the blending functions of the SST model. $F_{SST} = 0$ recovers the Strelets *et al.* model. F_1 and F_2 are the two blending functions of the SST model. F_2 shields more of the boundary layer and is therefore the preferred default. However, it should be noted that even F_2 does not completely eliminate the problem, but reduces it by an order of magnitude, $\triangle_s < c\,\delta$ where c is the order of 0.1.

2.3 Pseudo-Compressibility Method

One of the early techniques proposed for solving the incompressible Navier-Stokes equations in primitive variable form was the artificial compressibility method of Chorin [54]. In this method, the continuity equation is modified to include an artificial compressibility term that vanishes when the steady-state solution is reached. With the addition of this term to the continuity equation, the resulting Navier-Stokes equations are a mixed set of hyperbolic-parabolic equations, which can be solved using a standard time-dependent approach. The continuity equation is replaced by

$$\frac{\partial \rho^*}{\partial \tau} + \frac{\partial u_k}{\partial x_k} = 0 \qquad (2.21)$$

where ρ^* is an artificial density and τ is a fictitious time that is analogous to real time in a compressible flow. The artificial density is related to the pressure by the artificial equation of state

$$p^* = \beta \rho^* \qquad (2.22)$$

where β is the artificial compressibility factor.

To relate the pressure fields with the velocity fields, the artificial compressibility relation is introduced by adding a pseudo-time derivative of pressure to the continuity equation as

$$\frac{\partial p}{\partial \tau} = -\beta \nabla \cdot u \qquad (2.23)$$

The time derivation term in equation (2.4) is differenced using a backward second-order three-point implicit formula and moved to the right-hand side of the equation:

$$0 = -\frac{1.5 u_i^{n+1} - 2 u_i^n + 0.5 u_i^{n-1}}{\Delta t} - \hat{r}^{n+1} \qquad (2.24)$$

where $\varDelta t$ is the physical time step and the superscript n denotes the time level. To get the solution of equation (2.24) which satisfies equation

23

(2.3) at the physical time level $n+1$, the iterations will be performed until u_i^{n+1} is divergence free. The velocity field and pressure field will be modified during the iteration procedure to satisfy both equation (2.3) and (2.24). But, as the time-derivative term is absent from equation (2.3), it is not possible to update the pressure field. To relate the pressure field with the velocity field, the following pseudo-compressibility relation is introduced:

$$\frac{\partial \hat{p}^{n+1}}{\partial \tau} = -\beta \left[\frac{\partial}{\partial x} u + \frac{\partial}{\partial y} v + \frac{\partial}{\partial z} w \right]^{n+1} \tag{2.25}$$

Iteration will be performed on equation (2.25) as pseudo-time increases. Also a pseudo-time derivative of velocity is added to the left-hand side of equation (2.25):

$$\frac{\partial u_i^{n+1}}{\partial \tau} = -\frac{1.5 u_i^{n+1} - 2 u_i^{n} + 0.5 u_i^{n-1}}{\Delta t} - \hat{r}^{n+1} \tag{2.26}$$

Then, equation (2.25) and equation (2.26) can be combined into one equation and it is written in a vector form as follows:

$$\frac{\partial Q^{n+1}}{\partial \tau} = -R^{n+1} - S^{n+1} \tag{2.27}$$

where

$$R^{n+1} = \left(\frac{\partial}{\partial x}\left(E^n - E_v^n \right) + \frac{\partial}{\partial y}\left(F^n - F_v^n \right) + \frac{\partial}{\partial z}\left(G^n - G_v^n \right) \right)$$

$$Q = \begin{bmatrix} p \\ u \\ v \\ w \\ k \\ \omega \end{bmatrix} \quad E = \begin{bmatrix} \beta u \\ u^2 + p \\ uv \\ uw \\ uk \\ u\omega \end{bmatrix} \quad F = \begin{bmatrix} \beta v \\ vu \\ v^2 + p \\ vw \\ vk \\ v\omega \end{bmatrix} \quad G = \begin{bmatrix} \beta w \\ wu \\ wv \\ w^2 + p \\ wk \\ w\omega \end{bmatrix}$$

$$E_v = \frac{1}{\text{Re}} \begin{bmatrix} 0 \\ \hat{\tau}_{xx} \\ \hat{\tau}_{xy} \\ \hat{\tau}_{xz} \\ \left(\nu + \sigma_k \nu_t \right)\dfrac{\partial k}{\partial x} \\ \left(\nu + \sigma_\omega \nu_t \right)\dfrac{\partial \omega}{\partial x} \end{bmatrix} \qquad F_v = \frac{1}{\text{Re}} \begin{bmatrix} 0 \\ \hat{\tau}_{yx} \\ \hat{\tau}_{yy} \\ \hat{\tau}_{yz} \\ \left(\nu + \sigma_k \nu_t \right)\dfrac{\partial k}{\partial y} \\ \left(\nu + \sigma_\omega \nu_t \right)\dfrac{\partial \omega}{\partial y} \end{bmatrix}$$

$$G_v = \frac{1}{\text{Re}} \begin{bmatrix} 0 \\ \hat{\tau}_{zx} \\ \hat{\tau}_{zy} \\ \hat{\tau}_{zz} \\ \left(\nu + \sigma_k \nu_t \right)\dfrac{\partial k}{\partial z} \\ \left(\nu + \sigma_\omega \nu_t \right)\dfrac{\partial \omega}{\partial z} \end{bmatrix}$$

$$S^{n+1} = \frac{I_m}{\Delta t}\left(1.5Q^{n+1} - 2Q^n + 0.5Q^{n-1} \right)$$

$$I_m = diag[0,1,1,1,1]$$

As additional time scale is introduced to make use of the pseudo-compressibility method for unsteady problems, this procedure is called the method of dual time stepping. At each physical time level $n+1$, equation (2.27) will be solved as pseudo-time goes on until convergence is obtained.

The flux Jacobian matrices, have three different eigenvalues as will be shown in next chapter. For higher Reynolds number, the flow is predominated by convection. Equation (2.27) is hyperbolic in space and pseudo-time in the limit of Re→∞. The physical-time step term behaves like a source term to the hyperbolic equation. Thus, the upwind differencing methods developed for the hyperbolic system of equations of the compressible flow problems can be used to discretize the inviscid flux terms.

For the steay-state calculation, $\varDelta t$ is set to infinity and the quantities at physical time levels $n-1$ and n can be set to the freestream conditions. If the steady-state solution at physical time level $n+1$ is different from the freestream condition, which is the condition for all calculations, the source-like term will vanish. Then equation (2.27) is simplified for the steady-state calculation by dropping the superscript $n+1$ as:

$$\frac{\partial \hat{Q}}{\partial \tau} = -\hat{R} \qquad (2.28)$$

The governing equation for the steady-stat calculation is very easily derived from the time-accurate formulation by dropping the source-like term, and the resulting equation is exactly the same with the equation derived for the steady-state calculation only by others. The steady-state solution is

calculated with the unsteady solver by neglecting one term and proceeding in one physical time step with the time step Δt of infinity.

2.4 Transformation of the Incompressible Navier-Stokes Equations with Turbulence Model

The three-dimensional, incompressible Navier-Stokes equations coupled with two-equation turbulence model are non-dimensionalized by freestream conditions and the characteristic length:

$$
\begin{aligned}
u_i^* &= \frac{u_i}{u_\infty}, \quad p_i^* = \frac{\hat{p}}{p_\infty u_\infty^2} \quad , \quad v^* = \frac{v}{v_\infty} \\
v_t^* &= \frac{v_t}{v_\infty} \quad , \quad x_i^* = \frac{x_i}{L} \quad , \quad t^* = \frac{t}{Lu_\infty}
\end{aligned}
\tag{2.29}
$$

Then, the incompressible Navier-Stokes equations couple with the k-ω SST model can be written in Cartesian coordinates as

$$
\frac{\partial Q}{\partial \tau} = -\left[\frac{\partial}{\partial x}(E - E_v) + \frac{\partial}{\partial y}(F - F_v) + \frac{\partial}{\partial z}(G - G_v) \right] + S_T - S
\tag{2.30}
$$

where

$$
Q = \begin{bmatrix} p \\ u \\ v \\ w \\ k \\ \omega \end{bmatrix}
\qquad
E = \begin{bmatrix} \beta u \\ u^2 + p \\ uv \\ uw \\ uk \\ u\omega \end{bmatrix}
\qquad
F = \begin{bmatrix} \beta v \\ vu \\ v^2 + p \\ vw \\ vk \\ v\omega \end{bmatrix}
\qquad
G = \begin{bmatrix} \beta w \\ wu \\ wv \\ w^2 + p \\ wk \\ w\omega \end{bmatrix}
$$

$$
E_v = \frac{1}{\mathrm{Re}} \begin{bmatrix} 0 \\ \hat{\tau}_{xx} \\ \hat{\tau}_{xy} \\ \hat{\tau}_{xz} \\ \left(\nu + \sigma_k \nu_t\right)\dfrac{\partial k}{\partial x} \\ \left(\nu + \sigma_\omega \nu_t\right)\dfrac{\partial \omega}{\partial x} \end{bmatrix}
\qquad
F_v = \frac{1}{\mathrm{Re}} \begin{bmatrix} 0 \\ \hat{\tau}_{yx} \\ \hat{\tau}_{yy} \\ \hat{\tau}_{yz} \\ \left(\nu + \sigma_k \nu_t\right)\dfrac{\partial k}{\partial y} \\ \left(\nu + \sigma_\omega \nu_t\right)\dfrac{\partial \omega}{\partial y} \end{bmatrix}
$$

$$
G_v = \frac{1}{\mathrm{Re}} \begin{bmatrix} 0 \\ \hat{\tau}_{zx} \\ \hat{\tau}_{zy} \\ \hat{\tau}_{zz} \\ \left(\nu + \sigma_k \nu_t\right)\dfrac{\partial k}{\partial z} \\ \left(\nu + \sigma_\omega \nu_t\right)\dfrac{\partial \omega}{\partial z} \end{bmatrix}
$$

$$
S_T = \begin{bmatrix} 0 \\ 0 \\ 0 \\ 0 \\ \dfrac{\tau_{ij}}{\mathrm{Re}}\dfrac{\partial u_i}{\partial x_j} - \beta^* \omega k \\ \gamma \nu_t \tau_{ij}\dfrac{\partial u_i}{\partial x_j}\mathrm{Re} - \beta \omega^2 + 2(1 - F_1)\sigma_{\omega_2}\dfrac{1}{\omega}\dfrac{\partial k}{\partial x_j}\dfrac{\partial \omega}{\partial x_j} \end{bmatrix}
$$

$$S = \frac{1}{\Delta t} \begin{bmatrix} 0 \\ 1.5u^{n+1} - 2u^n + 0.5u^{n-1} \\ 1.5v^{n+1} - 2v^n + 0.5v^{n-1} \\ 1.5w^{n+1} - 2w^n + 0.5w^{n-1} \\ 1.5k^{n+1} - 2k^n + 0.5k^{n-1} \\ 1.5\omega^{n+1} - 2\omega^n + 0.5\omega^{n-1} \end{bmatrix}$$

The Eq. (2.30) is transformed in generalized curvilinear coordinates as

$$\frac{1}{J}\frac{\partial Q}{\partial \tau} = -\left[\frac{\partial}{\partial \xi}\left(\hat{E} - \hat{E}_v\right) + \frac{\partial}{\partial \eta}\left(\hat{F} - \hat{F}_v\right) + \frac{\partial}{\partial \zeta}\left(\hat{G} - \hat{G}_v\right) \right] + \hat{S}_T - \hat{S} \qquad (2.31)$$

where

$$\hat{E} = \frac{1}{J}\left(\xi_x E + \xi_y F + \xi_z G\right) = \frac{1}{J}\begin{bmatrix} \beta U \\ uU + \xi_x p \\ vU + \xi_y p \\ wU + \xi_z p \\ kU \\ \omega U \end{bmatrix}$$

$$\hat{F} = \frac{1}{J}\left(\eta_x E + \eta_y F + \eta_z G\right) = \frac{1}{J}\begin{bmatrix} \beta V \\ uV + \eta_x p \\ vV + \eta_y p \\ wV + \eta_z p \\ kV \\ \omega V \end{bmatrix}$$

$$\hat{G} = \frac{1}{J}\left(\zeta_x E + \zeta_y F + \zeta_z G\right) = \frac{1}{J}\begin{bmatrix} \beta W \\ uW + \zeta_x p \\ vW + \zeta_y p \\ wW + \zeta_z p \\ kW \\ \omega W \end{bmatrix}$$

$$\hat{E}_v = \frac{1}{J}\left(\xi_x E_v + \xi_y F_v + \xi_z G_v\right) = \frac{1}{J}\frac{1}{\mathrm{Re}}\begin{bmatrix} 0 \\ \xi_x \hat{\tau}_{xx} + \xi_y \hat{\tau}_{yx} + \xi_z \hat{\tau}_{zx} \\ \xi_x \hat{\tau}_{xy} + \xi_y \hat{\tau}_{yy} + \xi_z \hat{\tau}_{zy} \\ \xi_x \hat{\tau}_{xz} + \xi_y \hat{\tau}_{yz} + \xi_z \hat{\tau}_{zz} \\ \left(\nu + \sigma_k \nu_t\right)\left(\xi_x k_x + \xi_y k_y + \xi_z k_z\right) \\ \left(\nu + \sigma_\omega \nu_t\right)\left(\xi_x \omega_x + \xi_y \omega_y + \xi_z \omega_z\right) \end{bmatrix}$$

$$\hat{F}_v = \frac{1}{J}\left(\eta_x E + \eta_y F + \eta_z G\right) = \frac{1}{J}\frac{1}{\mathrm{Re}}\begin{bmatrix} 0 \\ \eta_x \hat{\tau}_{xx} + \eta_y \hat{\tau}_{yx} + \eta_z \hat{\tau}_{zx} \\ \eta_x \hat{\tau}_{xy} + \eta_y \hat{\tau}_{yy} + \eta_z \hat{\tau}_{zy} \\ \eta_x \hat{\tau}_{xz} + \eta_y \hat{\tau}_{yz} + \eta_z \hat{\tau}_{zz} \\ \left(\nu + \sigma_k \nu_t\right)\left(\eta_x k_x + \eta_y k_y + \eta_z k_z\right) \\ \left(\nu + \sigma_\omega \nu_t\right)\left(\eta_x \omega_x + \eta_y \omega_y + \eta_z \omega_z\right) \end{bmatrix}$$

$$\hat{G}_v = \frac{1}{J}\left(\zeta_x E + \zeta_y F + \zeta_z G\right) = \frac{1}{J}\frac{1}{\mathrm{Re}}\begin{bmatrix} 0 \\ \zeta_x \hat{\tau}_{xx} + \zeta_y \hat{\tau}_{yx} + \zeta_z \hat{\tau}_{zx} \\ \zeta_x \hat{\tau}_{xy} + \zeta_y \hat{\tau}_{yy} + \zeta_z \hat{\tau}_{zy} \\ \zeta_x \hat{\tau}_{xz} + \zeta_y \hat{\tau}_{yz} + \zeta_z \hat{\tau}_{zz} \\ \left(\nu + \sigma_k \nu_t\right)\left(\zeta_x k_x + \zeta_y k_y + \zeta_z k_z\right) \\ \left(\nu + \sigma_\omega \nu_t\right)\left(\zeta_x \omega_x + \zeta_y \omega_y + \zeta_z \omega_z\right) \end{bmatrix}$$

$$\hat{S}_T = \frac{1}{J} S_T = \frac{1}{J} \begin{bmatrix} 0 \\ 0 \\ 0 \\ 0 \\ \dfrac{\tau_{ij}}{\mathrm{Re}} \dfrac{\partial u_i}{\partial x_j} - \beta^* \omega k \\ \gamma \nu_t \tau_{ij} \dfrac{\partial u_i}{\partial x_j} \mathrm{Re} - \beta \omega^2 + 2(1-F_1)\sigma_{\omega_2} \dfrac{1}{\omega} \dfrac{\partial k}{\partial x_j} \dfrac{\partial \omega}{\partial x_j} \end{bmatrix}$$

$$\hat{S} = \frac{1}{J} \frac{1}{\Delta t} \begin{bmatrix} 0 \\ 1.5u^{n+1} - 2u^n + 0.5u^{n-1} \\ 1.5v^{n+1} - 2v^n + 0.5v^{n-1} \\ 1.5w^{n+1} - 2w^n + 0.5w^{n-1} \\ 1.5k^{n+1} - 2k^n + 0.5k^{n-1} \\ 1.5\omega^{n+1} - 2\omega^n + 0.5\omega^{n-1} \end{bmatrix}$$

$$U = \xi_x u + \xi_y v + \xi_z w$$

$$V = \eta_x u + \eta_y v + \eta_z w$$

$$W = \zeta_x u + \zeta_y v + \zeta_z w$$

2.5 Space Discritizaion Method

2.5.1 Differencing of Inviscid Flux Terms

The inviscid flux terms in the ξ, η, and ζ directions in Eq. (2.31) are discretized using a finite difference method as follows:

$$\left(\frac{\partial E}{\partial \xi} + \frac{\partial F}{\partial \eta} + \frac{\partial G}{\partial \zeta} \right)_{i,j,k}$$

$$= \tilde{E}_{i+\frac{1}{2},j,k} - \tilde{E}_{i-\frac{1}{2},j,k} + \tilde{F}_{i,j+\frac{1}{2},k} - \tilde{F}_{i,j-\frac{1}{2},k} + \tilde{G}_{i,j,+\frac{1}{2}} - \tilde{G}_{i,j,k-\frac{1}{2}} \tag{2.32}$$

where $\tilde{E}$, $\tilde{F}$, and $\tilde{G}$ are the modified fluxes, and i, j, and k are spatial indices. The finite difference method is very similar to a semi-discrete finite volume method which is based on the local flux balance of each cell. But in a finite difference method, the metrics of the transformation and the dependent variables are defined at mesh points instead of at cell face.

As the discretized equation, Eq. (2.32), is in a central differencing form which is non-dissipative by itself, the modified fluxes should include numerical dissipation models which are explicitly added to the physical flux terms:

$$\tilde{E}_{i+\frac{1}{2},j,k} = \frac{1}{2}\left(\hat{E}_{i+1,j,k} + \hat{E}_{i,j,k} \right) - \hat{D}_{i+\frac{1}{2},j,k},$$

$$\tilde{F}_{i,j+\frac{1}{2},k} = \frac{1}{2}\left(\hat{F}_{i,j+1,k} + \hat{F}_{i,j,k} \right) - \hat{D}_{i,j+\frac{1}{2},k}, \tag{2.33}$$

$$\tilde{G}_{i,j,k+\frac{1}{2}} = \frac{1}{2}\left(\tilde{G}_{i,j,k+1} + \tilde{G}_{i,j,k} \right) - \hat{D}_{i,j,k+\frac{1}{2}}.$$

The dissipation models are often called filters, since they work like low pass filters which damp out high frequency modes and suppress the tendency for odd and even point decoupling.

Spatial differencing can be either central or upwind differencing, depending on the numerical dissipation model in Eq. (2.33). The dissipation coefficient for a system of equations must be a matrix to meet the requirement of unwinding, and a scalar coefficient can be used for central differencing. The order of accuracy of the dissipation model will approach first order if discontinuities are present. However, since there is no discontinuity for incompressible flows, such as shock waves, the accuracy should be higher than first order.

2.5.2 Upwind Differencing Method

Upwind differencing simulates the wave propagation properties of hyperbolic equations and automatically suppresses unnecessary oscillations. For incompressible flows, the inviscid fluxes are not homogeneous of degree one in the state vector Q, that is, the following relations do not hold as for compressible flows:

$$\hat{E} = \hat{A}Q, \quad \hat{F} = \hat{B}Q, \quad \hat{G} = \hat{C}Q \qquad (2.34)$$

Hence, the usual flux vector splitting methods does not work here. Therefore, the inviscid fluxes are upwind-differenced using a flux-difference splitting based on Osher's upwind differencing scheme [55].

First-order accuracy in space can be obtained by defining the numerical dissipation model in equation (2.34) as

33

$$\hat{D}_{i+1/2} = \frac{1}{2}\left(\Delta \hat{E}^{+}_{i+1/2} - \Delta \hat{E}^{-}_{i+1/2}\right), \tag{2.35}$$

where $\Delta \hat{E}^{\pm}$ is the flux across positive or negative traveling waves and the subscript j and k are dropped for simplicity. The same method can be applied to the η and ζ direction terms. The flux difference is taken as

$$\Delta \hat{E}^{\pm}_{i+1/2} = \hat{A}^{\pm}\left(\overline{Q}\right)\!\Delta Q_{i+1/2}, \tag{2.36}$$

where the flux difference is evaluated at the midpoint by using the arithmetic average of Q:

$$\overline{Q} = \frac{Q_{i+1} - Q_i}{2}, \tag{2.37}$$

and the $\varDelta Q$ term is given by

$$\Delta Q_{i+1/2} = Q_{i+1} - Q_i \tag{2.38}$$

For three-dimensional problems, a similarity transformation for the Jacobian matrix given in Eq. (2.36) is introduced as

$$\hat{A}_i = X_i \Lambda_i X_i^{-1} \tag{2.39}$$

34

where

$$\Lambda = diag\left[\lambda_1, \lambda_2, \lambda_3, \lambda_4\right]$$

$$\lambda_{1,2} = \theta + k_t \qquad (2.40)$$

$$\lambda_{3,4} = \theta + \frac{1}{2}k_t \pm c$$

and c is the scaled artificial speed of sound given by

$$c = \sqrt{\left(\theta + \frac{1}{2}k_t\right)^2 + \beta\left(k_x^2 + k_y^2 + k_z^2\right)},$$

$$\theta = k_x u + k_y v + k_z w, \qquad (2.41)$$

$$k_x = \frac{1}{J}\frac{\partial \xi_i}{\partial x}, \quad k_y = \frac{1}{J}\frac{\partial \xi_i}{\partial y}, \quad k_z = \frac{1}{J}\frac{\partial \xi_i}{\partial z}, \quad k_t = \frac{1}{J}\frac{\partial \xi_i}{\partial t},$$

$$\xi_i = \xi, \eta, \zeta \text{ for } i = 1, 2, 3.$$

It should be noted that the subscript i here represents the coordinate direction. The matrix of the right eigenvectors is given by

$$X_i = \begin{bmatrix} 0 & 0 & \beta(c - k_t/2) & -\beta(c + k_t/2) \\ x_k & x_{kk} & u\lambda_3 + \beta k_x & u\lambda_4 + \beta k_x \\ y_k & y_{kk} & v\lambda_3 + \beta k_y & u\lambda_4 + \beta k_y \\ z_k & z_{kk} & w\lambda_3 + \beta k_z & u\lambda_4 + \beta k_z \end{bmatrix} \quad 0 \qquad (2.42)$$

$$x_k = \frac{\partial x}{\partial \xi_{i+1}}, \quad x_{kk} = \frac{\partial x}{\partial \xi_{i+2}}$$

$$\xi_{i+1} = \eta, \zeta, \xi \quad \text{for} \quad i = 1, 2, 3 ,$$

$$\xi_{i+2} = \zeta, \xi, \eta \quad \text{for} \quad i = 1, 2, 3 ,$$

and its inverse is given by

$$X_i^{-1} = \frac{1}{c^2 - k_t^2 / 4}$$

$$\begin{bmatrix}
x_{kk}(k_z v - k_y w) + y_{kk}(k_x w - k_z u) + z_{kk}(k_y u - k_x v) \\
x_k(k_y w - k_z v) + y_k(k_z u - k_x w) + z_k(k_x v - k_y u) \\
-\lambda_4(c + k_t / 2)/(2\beta c) \\
-\lambda_3(c - k_t / 2)/(2\beta c) \\
\\
y_{kk}(\lambda_1 w + \beta k_z) - z_{kk}(\lambda_1 v + \beta k_y) \\
-y_k(\lambda_1 w + \beta k_z) + z_k(\lambda_1 v + \beta k_y) \\
k_x(c + k_t / 2)/(2c) \\
k_x(c - k_t / 2)/(2c) \\
\\
z_{kk}(\lambda_1 u + \beta k_x) - x_{kk}(\lambda_1 w + \beta k_z) \\
-z_k(\lambda_1 u + \beta k_x) + x_k(\lambda_1 w + \beta k_z) \\
k_y(c + k_t / 2)/(2c) \\
k_y(c - k_t / 2)/(2c) \\
\\
x_{kk}(\lambda_1 v + \beta k_y) - y_{kk}(\lambda_1 u + \beta k_x) \\
-x_k(\lambda_1 v + \beta k_y) + y_k(\lambda_1 u + \beta k_x) \\
k_z(c + k_t / 2)/(2c) \\
k_z(c - k_t / 2)/(2c)
\end{bmatrix} \qquad (2.43)$$

The diagonal matrix Λ_i can be split into positive and negative running characteristics which have only positive and negative diagonal entries, respectively.

$$\left|\Lambda_i\right| = diag\left[\left|\lambda_1\right|, \left|\lambda_2\right|, \left|\lambda_3\right|, \left|\lambda_4\right|\right]$$

$$\Lambda_i = \Lambda_i^+ + \Lambda_i^-$$

$$\Lambda_i^+ = \frac{\Lambda_i + \left|\Lambda_i\right|}{2}$$

$$\Lambda_i^- = \frac{\Lambda_i - \left|\Lambda_i\right|}{2}$$

(2.44)

The A^+ and A^- matrices are computed by decomposing the diagonal matrix in Eq. (2.39) using the relations in Eq. (2.44):

$$\hat{A}_i = X_i\left(\Lambda_i^+ + \Lambda_i^-\right)X_i^{-1} = X_i\Lambda_i^+ X_i^{-1} + X_i\Lambda_i^- X_i^{-1} \qquad (2.45)$$

Thus we get

$$\hat{A}_i^+ = X_i\Lambda_i^+ X_i^{-1}$$
$$\hat{A}_i^- = X_i\Lambda_i^- X_i^{-1}$$

(2.46)

If we define an absolute Jacobian matrix as

$$\left|\hat{A}_i\right| = X_i\left|\Lambda_i\right|X_i^{-1} \qquad (2.47)$$

then we get

$$\left|\hat{A}_i\right| = \hat{A}_i^+ - \hat{A}_i^- \tag{2.48}$$

with Eq. (2.48), Eq. (2.35) can now be rewritten as

$$\hat{D}_{i+1/2} = \frac{1}{2}\left|\hat{A}_{i+1/2}\right|(Q_{i+1} - Q_i) \tag{2.49}$$

2.5.3 Low Dissipative Upwind Differencing Method

To reduce excessive numerical dissipation in a non-flow-aligned grid system, Kim *et al.* introduced a new spatial discretization technique [56]. Through the analysis of TVD limiters, a criterion was proposed to predict cell-interface states accurately both in smooth region and in discontinuous region. According to the criterion, they developed a new way of re-evaluating the cell-interface convective flux in AUSM-type methods. Considering the regions where LES computation is adopted of DES, upwind schemes which are implemented in most solvers seem to be too dissipative for LES [57]. Therefore, the idea of the newly formulated AUSM type flux for multi-dimensional flows is adopted as:

If $(\Phi_R - \Phi_L)(\Phi_{L,\text{sup}erbee} - 0) \le 0$; $\Phi_{L,1/2} = \Phi_L$

If $(\Phi_R - \Phi_L)(\Phi_{L,\text{sup}erbee} - 0) > 0$;

$$\Phi_{L,1/2} = \Phi_L + \frac{\max\left[0,(\Phi_R - \Phi_L)(\Phi_{L,\mathrm{superbee}} - \Phi_L)\right]}{(\Phi_R - \Phi_L)\left|\Phi_{L,\mathrm{superbee}} - \Phi_L\right|} \min\left[\frac{\left|\Phi_R - \Phi_L\right|}{2}, \left|\Phi_{L,\mathrm{superbee}} - \Phi_L\right|\right]$$

$$\Phi_{R,1/2} = \Phi_R + \frac{\max\left[0,(\Phi_L - \Phi_R)(\Phi_{R,\mathrm{superbee}} - \Phi_R)\right]}{(\Phi_L - \Phi_R)\left|\Phi_{R,\mathrm{superbee}} - \Phi_R\right|} \min\left[\frac{\left|\Phi_L - \Phi_R\right|}{2}, \left|\Phi_{R,\mathrm{superbee}} - \Phi_R\right|\right]$$

$$(2.50)$$

where

$$\Phi_{L,1/2} = q_{i+1/2}^{Left}, \quad \Phi_{R,1/2} = q_{i+1/2}^{Right} \quad (q : \text{primitive variables})$$

$$\Phi_{L,\mathrm{superbee}} = \Phi_{real,i+1/2} + \frac{\Delta x^2}{6}\Phi'' + O(\Delta x^3)$$

$$\Phi_{R,\mathrm{superbee}} = \Phi_{real,i+1/2} - \frac{\Delta x^2}{3}\Phi'' + O(\Delta x^3)$$

2.5.4 Higher Order Spatial Accuracy

In order to obtain higher order spatial accuracy, a Monotone Upstream-centered Schemes for Conservation Laws (MUSCL [58]) interpolation is adopted as:

$$q_{i+1/2}^{Left} = q_i + \frac{1}{4}\left[(1-\kappa)(q_i - q_{i-1}) + (1+\kappa)(q_{i+1} - q_i)\right]$$

$$q_{i+1/2}^{Right} = q_i - \frac{1}{4}\left[(1+\kappa)(q_{i+1} - q_i) + (1-\kappa)(q_{i+2} - q_{i+1})\right]$$

$$(2.51)$$

where q denotes the primitive variables. For constant k=1/3, the order of spatial accuracy is third, and the second order accuracy for k=-1, 0, 1. Especially for k=1, it becomes a central-difference scheme of second order.

Because the MUSCL scheme is developed in the one-dimensional approach, it is insufficient to control oscillation near shock discontinuity in two- or three-dimensions. To overcome this limitation, the Multi-dimensional Limiting Process (MLP) [59] is also adopted. The vertex point value is expressed in terms of variations across the cell-interface, and by adopting the multi-dimensional restriction coefficient α, the MLP derives the multi-dimensional limiting function. The MLP scheme is

$$
\begin{aligned}
q_{i+1/2}^{Left} &= q_i + \frac{1}{2}\phi(r_{Left})\vartriangle q_{i-1/2} \\
q_{i+1/2}^{Right} &= q_i - \frac{1}{2}\phi(r_{Right})\vartriangle q_{i+3/2}
\end{aligned}
\tag{2.52}
$$

where

$$
r_{Left} = \frac{\vartriangle q_{i+1/2}}{\vartriangle q_{i-1/2}}, \;\; r_{Right} = \frac{\vartriangle q_{i+1/2}}{\vartriangle q_{i+3/2}}
$$

$$
\phi(r) = \max(0, \min(\alpha, \alpha r, \beta))
$$

$$
1 \le \alpha \le \min\left[2, \frac{2\max(1, r_{Left,j})(1+\max(0, \tan\overline{\theta}_{j+1} / r_{Right,j+1}))}{1+\tan\tilde{\theta}_j} \right]
$$

$$
\tan\overline{\theta}_j = \frac{\vartriangle q_x^+}{\vartriangle q_y^+}, \;\; \tan\tilde{\theta}_j = \frac{\vartriangle q_{i+1/2,j}}{\vartriangle q_{i,j+1/2}}
$$

The $\triangle q_{x,y}^{\pm}$ is variation from center point to the cell-interface. The coefficient β is the local slope evaluated by a higher order polynomial interpolation, which is determined by the third-order polynomial interpolation as follows:

$$\beta_{Left} = \frac{1 + 2r_{Left,i}}{3}, \quad \beta_{Right} = \frac{1 + 2r_{Right,i+1}}{3} \tag{2.53}$$

and the fifth-order polynomial interpolation as follows:

$$\beta_{Left} = \frac{-2/r_{Left,i} + 11 + 24r_{Left,i} - 3r_{Left,i}r_{Left,i+1}}{30}$$

$$\beta_{Right} = \frac{-2/r_{Right,i+2} + 11 + 24r_{Right,i+1} - 3r_{Right,i+1}r_{Right,i}}{30} \tag{2.54}$$

2.6   Time Integration Method

In this chapter, the implicit methods to solve the pseudo-time equation, equation (2.26), is presented. A first-order Euler implicit formula is used for pseudo-time derivative to form the matrix equation. The next consideration is the formation of the Jacobian matrix of the residual vector of the flux terms required for the implicit side of the resulting equation. However, the exact Jacobian of the flux vectors is very costly to form. Instead, an approximate Jacobian of the residual vector can be used with

different levels of approximation. Then, the matrix equation is solved using LU symmetric Gauss-Seidel (SGS) relaxation scheme.

2.6.1 Dual Time Stepping

For time-accurate unsteady problems, pseudo-time sub-iteration strategy is adopted to solve the unsteady, incompressible systems given by:

$$\frac{1}{J}\frac{\partial Q}{\partial t} = -\hat{R} \quad . \tag{2.55}$$

The time derivative term is differenced using a backward second-order three-point implicit formula and moved to the right-hand side of the equation:

$$0 = -\frac{1.5Q^{n+1} - 2Q^n + 0.5Q^{n-1}}{J\Delta t} - \hat{R}^{n+1} \tag{2.56}$$

where a superscript n denotes the physical time iteration level.

A pseudo-time derivative of Q is added on the left-hand side of Eq. (2.56):

$$\frac{1}{J}\frac{\partial Q^{n+1}}{\partial \tau} = -\hat{R}^{n+1} - \frac{1.5Q^{n+1} - 2Q^n + 0.5Q^{n-1}}{J\Delta t} = -\hat{R}^{n+1} - \hat{S}^{n+1} \tag{2.57}$$

Since the first-order discretization has better convergence properties than higher-order in general, the pseudo-time derivative term is discretized using the first-order Euler implicit formula:

$$\frac{1}{J}\frac{Q^{n+1,m+1}-Q^{n+1,m}}{\Delta\tau}=-\hat{R}^{n+1,m+1}-\hat{S}^{n+1,m+1} \qquad (2.58)$$

where a superscript m denotes the pseudo-time iteration level. The time accuracy of the solution is necessary in terms of the physical time, but not in terms of the pseudo-time. Therefore, the dual time stepping method adopted here has second-order time accuracy. Now, Eq. (2.58) can be rewritten as by using a simple Taylor series expansion:

$$\left[\frac{1}{J\Delta\tau}+\left(\frac{\partial\hat{R}}{\partial Q}+\frac{\partial\hat{S}}{\partial Q}\right)^{n+1,m}\right]\Delta Q^{n+1,m}=-\hat{R}^{n+1,m}-\hat{S}^{n+1,m} \qquad (2.59)$$

For steady-state calculations, the source-like term S dropped from the equation because $\triangle t$ is set to infinity. Then Eq. (2.59) is simplified for the steady-state calculation as:

$$\frac{1}{J\Delta\tau}+\left[\frac{\partial\hat{R}}{\partial Q}\right]^{m}\Delta Q^{m}=-\hat{R}^{m}. \qquad (2.60)$$

2.6.2 Pseudo-Time Discretization

The system of governing equations, Eq. (2.58), can be rewritten as:

$$\frac{1}{J}\frac{\partial Q^{m+1}}{\partial \tau} + \left[\frac{\partial}{\partial \xi}\left(\hat{E} - \hat{E}_v\right) + \frac{\partial}{\partial \eta}\left(\hat{F} - \hat{F}_v\right) + \frac{\partial}{\partial \zeta}\left(\hat{G} - \hat{G}_v\right)\right]^{m+1} - \hat{S}_T^{m+1} + \hat{S}^{m+1} = 0$$

(2.61)

where the superscript n+1 is dropped for simplicity.

Consider a Taylor series expansion about pseudo-time level m as follows:

$$\hat{E}^{m+1} = \hat{E}^m + \left[\frac{\partial \hat{E}}{\partial Q}\right]^m \Delta Q^m + O(\Delta \tau^2) \cong \hat{E}^m + \hat{A}\Delta Q^m$$

(2.62)

In a similar fashion the other flux vectors can be linearized as:

$$\hat{F}^{m+1} \cong \hat{F}^m + \hat{B}\Delta Q^m$$
$$\hat{G}^{m+1} \cong \hat{G}^m + \hat{C}\Delta Q^m$$
$$\hat{S}_T^{\,m+1} \cong \hat{S}_T^{\,m} + \hat{D}_T\Delta Q^m$$

(2.63)

where

$$D_T = \frac{1}{J}diag\left[0,0,0,0,-2\beta^*\omega,-2\beta\omega\right]$$

(2.64)

44

The viscous flux Jacobian in the implicit part is neglected since it does not influence the solution's accuracy. Thus, the viscous flux vectors are approximated as follows:

$$\hat{E}_v^{m+1} \cong \hat{E}_v^m$$
$$\hat{F}_v^{m+1} \cong \hat{F}_v^m \qquad (2.65)$$
$$\hat{G}_v^{m+1} \cong \hat{G}_v^m$$

Substituting the above linearization in Eq. (2.61) to obtain

$$\frac{1}{J}\frac{\Delta Q^m}{\Delta \tau} + \left[\frac{\partial}{\partial \xi}\left(\hat{E}^m + \hat{A}\Delta Q^m \right) + \frac{\partial}{\partial \eta}\left(\hat{F}^m + \hat{B}\Delta Q^m \right) + \frac{\partial}{\partial \zeta}\left(\hat{G}^m + \hat{C}\Delta Q^m \right) \right]$$
$$- \left(\frac{\partial \hat{E}_v^m}{\partial \xi} + \frac{\partial \hat{F}_v^m}{\partial \eta} + \frac{\partial \hat{G}_v^m}{\partial \zeta} \right) - \hat{S}_T^m - \hat{D}_T \Delta Q^m + \hat{S}^{m+1} = 0$$

$$(2.66)$$

where

$$\Delta Q^m = Q^{m+1} - Q^m$$

$$\hat{S}^{m+1} \cong \hat{S}^m + \left[\frac{\partial \hat{S}}{\partial Q} \right]^m \Delta Q^m$$

Rewriting the Eq. (2.66)

$$\frac{I}{J}\frac{\Delta Q^m}{\Delta \tau} + \frac{\partial}{\partial \xi}\left(\hat{A}\Delta Q^m\right) + \frac{\partial}{\partial \eta}\left(\hat{B}\Delta Q^m\right) + \frac{\partial}{\partial \zeta}\left(\hat{C}\Delta Q^m\right) - \hat{D}_T\Delta Q^m + \left[\frac{\partial \hat{S}}{\partial Q}\right]^m \Delta Q^m$$

$$= -\left(\frac{\partial}{\partial \xi}\left(\hat{E} - \hat{E}_v\right) + \frac{\partial}{\partial \eta}\left(\hat{F} - \hat{F}_v\right) + \frac{\partial}{\partial \zeta}\left(\hat{G} - \hat{G}_v\right)\right)^m + \hat{S}_T^m - \hat{S}^m$$

$$(2.67)$$

and is factored as

$$\left(\frac{I}{J\Delta\tau} + \frac{\partial \hat{S}}{\partial Q} + \frac{\partial \hat{A}}{\partial \xi} + \frac{\partial \hat{B}}{\partial \eta} + \frac{\partial \hat{C}}{\partial \zeta} - \hat{D}_T\right)\Delta Q^m$$

$$= -\left(\frac{\partial}{\partial \xi}\left(\hat{E} + \hat{E}_v\right) + \frac{\partial}{\partial \eta}\left(\hat{F} + \hat{F}_v\right) + \frac{\partial}{\partial \zeta}\left(\hat{G} + \hat{G}_v\right)\right)^m + \hat{S}_T^m - \hat{S}^m = -\hat{R}^m$$

$$(2.68)$$

where I is the identity matrix and R stands for the residual vector including viscous terms. The flux Jacobian matrices are split according to the signs of the eigenvalues of the flux Jacobian matrices as:

$$\left(\frac{I_{tr}}{J} + \delta_\xi^+ \hat{A}^+ + \delta_\xi^- \hat{A}^- + \delta_\eta^+ \hat{B}^+ + \delta_\eta^- \hat{B}^- + \delta_\zeta^+ \hat{C}^+ + \delta_\zeta^- \hat{C}^- - \hat{D}_T\right)\Delta Q^m = -\hat{R}^m$$

$$(2.69)$$

where

$$I_{tr} = \frac{I}{\Delta\tau} + \frac{\partial S}{\partial Q} .$$

and δ denotes a finite difference operator in each direction.

2.6.3 LU-SGS Scheme

Yoon *et al.* [60] introduced an implicit algorithm based on a Lower-Upper factorization and Gauss-Seidel relaxation. Rewriting Eq. (2.69) in detail yields

$$\left[\frac{I_{tr}}{J} + \hat{A}_i^+ - \hat{A}_{i-1}^+ + \hat{A}_{i+1}^- - \hat{A}_i^- + \hat{B}_j^+ - \hat{B}_{j-1}^+ + \hat{B}_{j+1}^- - \hat{B}_j^- \right.$$
$$\left. + \hat{C}_k^+ - \hat{C}_{k-1}^+ + \hat{C}_{k+1}^- - \hat{C}_k^- - \hat{D}_T \right] \Delta Q^m = -\hat{R}_{i,j,k}^m \tag{2.70}$$

and Eq. (2.70) can be rewritten in a compact form as:

$$\left[\left(\frac{I_{tr}}{J} + \rho(\hat{A}) + \rho(\hat{B}) + \rho(\hat{C}) \right) I - \hat{D}_T - \hat{A}_{i-1}^+ + \hat{A}_{i+1}^- - \hat{B}_{j-1}^+ + \hat{B}_{j+1}^- - \hat{C}_{k-1}^+ + \hat{C}_{k+1}^- \right] \Delta Q^m$$
$$= -\hat{R}_{i,j,k}^m$$

$$\tag{2.71}$$

and the flux Jacobian matrices are split approximately to yield diagonal dominance as

$$\hat{A}^{\pm} = \frac{1}{2}\left(\hat{A} \pm \rho(\hat{A})\right), \hat{B}^{\pm} = \frac{1}{2}\left(\hat{B} \pm \rho(\hat{B})\right), \hat{C}^{\pm} = \frac{1}{2}\left(\hat{C} \pm \rho(\hat{C})\right)$$
$$\rho(\hat{A}) = \hat{A}_i^+ - \hat{A}_i^-, \rho(\hat{B}) = \hat{B}_i^+ - \hat{B}_i^-, \rho(\hat{C}) = \hat{C}_i^+ - \hat{C}_i^-$$
(2.72)

where $\rho(A) = \kappa \left| \lambda(A) \right|$ and κ denotes a constant that is between 1.01 and 1.5. In the present work, κ is given 1.1 for incompressible problems. Rewriting Eq. (2.71) yields

$$(r_{i,j,k}I - \hat{D}_T)\Delta Q^m - \hat{A}_{i-1}^+\Delta Q^m + \hat{A}_{i+1}^-\Delta Q^m - \hat{B}_{j-1}^+\Delta Q^m + \hat{B}_{j+1}^-\Delta Q^m$$
$$-\hat{C}_{k-1}^+\Delta Q^m + \hat{C}_{k+1}^-\Delta Q^m = -\hat{R}_{i,j,k}^m$$
(2.73)

where

$$r_{i,j,k} = \frac{1}{J\Delta\tau} + \rho(\hat{A}) + \rho(\hat{B}) + \rho(\hat{C})$$
(2.74)

The above factored equation is solved as a series of following lower and upper sweeps.

Lower sweep :

$$
\begin{aligned}
(r_{i,j,k}I - \hat{D}_T)\Delta Q_{i,j,k}^{*} &= -\hat{R}_{i,j,k}^{m} + \hat{A}_{i-1,j,k}^{+}\Delta \hat{Q}_{i-1,j,k}^{*} + \hat{B}_{i,j-1,k}^{+}\Delta \hat{Q}_{i,j-1,k}^{*} \\
&\quad + \hat{C}_{i,j,k-1}^{+}\Delta \hat{Q}_{i,j,k-1}^{*} - \hat{A}_{i+1,j,k}^{-}\Delta \hat{Q}_{i+1,j,k}^{*} \\
&\quad - \hat{B}_{i,j+1,k}^{-}\Delta \hat{Q}_{i,j+1,k}^{*} - \hat{C}_{i,j,k+1}^{-}\Delta \hat{Q}_{i,j,k+1}^{*} \\
&\approx -\hat{R}_{i,j,k}^{m} + \hat{A}_{i-1,j,k}^{+}\Delta \hat{Q}_{i-1,j,k}^{*} + \hat{B}_{i,j-1,k}^{+}\Delta \hat{Q}_{i,j-1,k}^{*} \qquad (2.75) \\
&\quad + \hat{C}_{i,j,k-1}^{+}\Delta \hat{Q}_{i,j,k-1}^{*} \\
&= DCV_{i,j,k}
\end{aligned}
$$

Upper sweep :

$$
\begin{aligned}
(r_{i,j,k}I - \hat{D}_T)\Delta \hat{Q}_{i,j,k}^{m} &= -\hat{R}_{i,j,k}^{m} + \hat{A}_{i-1,j,k}^{+}\Delta \hat{Q}_{i-1,j,k}^{m} + \hat{B}_{i,j-1,k}^{+}\Delta \hat{Q}_{i,j-1,k}^{m} \\
&\quad + \hat{C}_{i,j,k-1}^{+}\Delta \hat{Q}_{i,j,k-1}^{m} - \hat{A}_{i+1,j,k}^{-}\Delta \hat{Q}_{i+1,j,k}^{m} \\
&\quad - \hat{B}_{i,j+1,k}^{-}\Delta \hat{Q}_{i,j+1,k}^{m} - \hat{C}_{i,j,k+1}^{-}\Delta \hat{Q}_{i,j,k+1}^{m} \\
&\approx -\hat{R}_{i,j,k}^{m} + \hat{A}_{i-1,j,k}^{+}\Delta \hat{Q}_{i-1,j,k}^{*} + \hat{B}_{i,j-1,k}^{+}\Delta \hat{Q}_{i,j-1,k}^{*} \\
&\quad + \hat{C}_{i,j,k-1}^{+}\Delta \hat{Q}_{i,j,k-1}^{*} - \hat{A}_{i+1,j,k}^{-}\Delta \hat{Q}_{i+1,j,k}^{m} \qquad (2.76) \\
&\quad - \hat{B}_{i,j+1,k}^{-}\Delta \hat{Q}_{i,j+1,k}^{m} - \hat{C}_{i,j,k+1}^{-}\Delta \hat{Q}_{i,j,k+1}^{m} \\
&= DCV_{i,j,k} - \hat{A}_{i+1,j,k}^{-}\Delta \hat{Q}_{i+1,j,k}^{m} - \hat{B}_{i,j+1,k}^{-}\Delta \hat{Q}_{i,j+1,k}^{m} - \hat{C}_{i,j,k+1}^{-}\Delta \hat{Q}_{i,j,k+1}^{m}
\end{aligned}
$$

Consequently, the LU-SGS scheme can be written in the following form:

$$
LD^{-1}U\Delta Q^{m} = -R^{m} \qquad (2.77)
$$

2.7 Synthetic Jet Boundary Condition

Rumsey *et al.* reported that the velocity distributions near the orifice exit might exhibit some anomalies not captured or modeled by CFD, but they also mentioned at CFDVAL2004 that reasonably good qualitative results could be obtained compared to experimental results from the point of view of global flow features [61,62]. In addition, the 'top hat' condition neglecting the spatial variation of the jet was employed to obtain physically meaningful results [15,16]. Based on these results, suction/blowing type boundary condition proposed by Kral *et al.* [63] was adopted in the present work to model a synthetic jet actuator. Perturbation to the flow-field was introduced by the jet velocity as

$$\vec{u}_n(\xi = 0, \eta = 0, \zeta, t) = A_{jet} f(\zeta) \sin(\omega t) \vec{d}_{jet} \qquad (2.78)$$

where ξ denotes the stream-wise direction, η for the cross-slot direction. u_n is the velocity vector and d_{jet} is a unit vector in the jet direction. Spatial variation over the orifice was neglected and assumed as a top hat distribution ($f(\zeta)=1$) in the form. Pressure boundary condition at solid surface was obtained by the momentum equation ignoring viscous effects. The time harmonic velocity perturbation was considered and then the boundary condition becomes

$$\frac{\partial \overline{p}}{\partial \xi} = -\rho \frac{\partial \overline{u}_n}{\partial t} \qquad (2.79)$$

Chapter III

Flow Characteristics of Synthetic Jets

3.1 Two Types of Synthetic Jet Exit

Synthetic jets induce trains of vortex interactions. The alternating ejection and suction across the jet exit produces periodic vortices, which accompany the momentum transfer to an external flow field. The structure of a periodic vortex strongly influences momentum transfer, which, in turn, determines the performance of separation control. Since the exit configuration of a synthetic jet strongly affects the jet vortex structure, the assumption follows that the exit configuration of a synthetic jet is closely related to the flow control capability. The performance of synthetic jets essentially comes from the interactions of jet vortices with external flow fields. Therefore, geometric parameters that are critical to the formation of jet vortices, such as exit configuration, must be explored before determining the proper range of the key parameters.

In our previous work, Kim *et al.* [64] performed experimental and computational investigations on the characteristics of synthetic jets for different exit configurations under various flow conditions. They considered two types of exit configurations whether the vortex structure of exit is either a two-dimensional vortex pair or a three-dimensional vortex ring: one is a

conventional rectangular slot and the other is a series of circular holes. Comparative studies were then conducted for a quiescent condition, a cross flow field, and a forced separated flow. This study has revealed the numerous flow field characteristics produced by synthetic jets. At the same time, however, the vortex structures produced by interactions of a synthetic jet with external flow fields have not been fully understood. The present study expands on the work by Kim *et al.* and addresses flow characteristics of synthetic jets depending on the exit configuration under a cross flow condition.

From this perspective, two types of exit geometries are considered for two types of vortex structures: a rectangular type and a serial circular exit. The rectangular exit produces, except for the edge of the exit, a two-dimensional vortex pair, while the circular exit produces an axisymmetric vortex ring. However, if the vortex ring interacts with adjacent ones in serial circular jets, it may exhibit a three-dimensional structure. Since different vortex structures will yield different mixing effects, comparative studies on the two vortex structures are carried out while other parameters are kept the same.

Figure 3.1 shows the schematic of each exit configuration. The rectangular exit has a width of 0.6 mm and a span of 50 mm, and the circular exit has 17 circular holes, which is composed of 1.5 mm hole diameter and 1.5 mm hole gap. In order to maintain the same geometrical condition, the total exit area, the total jet momentum, and the span length were set the same for each jet configuration.

52

3.2   Code Validation

The cases of the conventional rectangular slot and the multiple serial circular exit were considered for code validation. The geometric details and experimental data can be found in Ref. 64. The Reynolds number of the circular hole diameter is 1000, the freestream velocity is 10 m/s, the jet frequency is fixed at 50 Hz, and the maximum velocity of the synthetic jet is 40 m/s. The synthetic jet boundary conditions can be determined from the flow condition.

The computational coordinate system is shown in Fig. 3.2. The X-direction is along the streamwise direction, the Y-direction is along the spanwise direction of the exit, and the Z-direction is along the normal direction from the wall. The origin of the coordinate is the center of the span. Figure 3.3 shows the computational domain and boundary conditions used in the simulation. The inlet of the flow domain was located 150 mm upstream of the jet exit, and the outlet was set at 450 mm downstream of the jet exit. The height and width of the computation domain were 300 mm and 250 mm, respectively.

Since the flow field was symmetric with respect to the XZ plane from the origin, only a half of the flow field was modeled to save the computational time. The inlet condition was specified using the steady mean velocity profiles of a fully turbulent incompressible flow. A symmetric boundary condition was used on the surface on the both side of the XZ plane.

The outlet pressure condition was employed at both the flow outlet domain and the surface opposite to the wall.

Verification study has been performed in term of grid refinement and time step sensitivity. To examine the grid refinement, three grid densities were considered for the rectangular and circular exits. From the comparison of the computed results depicted in Fig. 3.4a, the differences between fine mesh and medium mesh are less than 2%, which is thought to be adequate for reliable computations. Thus, mesh systems of 8 and 13 million grid points were considered for the rectangular exit and the circular exit, respectively. Using the chosen grid system, the time-step sensitivity was also examined. In order to maintain sufficient temporal accuracy, sub-iterations were conducted in pseudo-time until the maximum flow divergence of the converged solution at the fixed physical time became less than 1.0×10^{-5}. Three levels of different time steps were tested: 60, 90, and 120 steps per synthetic jet period. Figure 3.4b shows the velocity profiles according to the number of time steps. The computational differences between 90 and 120 time steps were less than 2 percent, indicating that 90 time steps could adequately resolve the time-dependent nature of the flow fields within the URANS formulation. Computed results were obtained after reaching a sufficient level of time-periodic behavior.

Figure 3.5 shows the distribution of the time-averaged velocity profiles of the boundary layers along the downstream direction in the rectangular and circular exits. The computed results show a reasonable agreement with experimental data. Therefore, the numerical simulation is

believed to be fully capable of simulating the behavior of synthetic jets for the cross flow condition.

3.3 Characteristics of Rectangular and Circular Exits

The whole results are divided into two parts: analysis of flow characteristics, and evaluation of effective shape for the rectangular and the multiple serial circular exits using synthetic jets. The objective of the first part is to understand the flow structures and the flow control effectiveness for rectangular and circular exits. In the second part, comparative studies were conducted according to the hole parameters of the circular exit. The results are obtained under the same operation conditions, such as jet frequency, total jet momentum. Though not presented here, the choice of the grid system and the time step was based on the resolution study, as in the case of the code validation.

3.3.1 Flow Structures

Figure 3.6 presents the results of the time-averaged vortical structures in cross flow interaction for the rectangular exit. In case of the rectangular exit, a long two-dimensional vortex pair is observed along the spanwise direction, and a semicircular vortex is seen at the end of the slot under quiescent conditions [64]. For the cross flow field, the vortex pair part negatively interacts with the free stream, which makes the vortex strength

weaker along X-direction and Z-direction. The semicircular vortex favorably interacts with the freestream to strengthen the initial vortex, and thus, it is able to survive longer than the vortex pair part and strongly affect the flow near the end of the slot. As a result of the interactions, a weak strength of the vortex pair part along the spanwise direction and a relatively strong strength of the semicircular vortex part near the slot end are observed.

On the other hand, the circular exit significantly changes the vortical structure from the slot center to the slot end, as shown in Fig. 3.7. For the quiescent condition, the circular exit yields vortex rings at each hole and the vorticies exhibits an additional three-dimensional flow structure by the interaction of serial vortex rings along the spanwise direction. [64]. Through the three-dimensional nature of the interaction between jet vortices and the freesteam in serial circular jets, the overall vortical structures are stronger and relatively more sustainable, and its influence on the flow field is much more visible than rectangular case. This means that the circular exit affects local flow characteristics more widely than the rectangular exit.

Figures 3.8 and 3.9 present the evolution of a jet vortex formation and streamlines. The time sequences of the iso-surface vorticity and streamlines provide insight on the interaction between the synthetic jet and the freestream. During the blowing phase, flows are separated at the edge of the exit, and form a vortex structure. The vortex structure moves away through the cross flow interactions, and affects the flow characteristics afterward. During the suction phase, the suction component mainly exists in

the near field of the jet exit, while the blowing component persists in the far field region.

As shown in Figs. 3.8e-f and 3.9e-f, the flow structures of the two exits are not significantly different in suction phase, which means that the suction effect is minor than the blowing component. The overall flow structures (or patterns of streamlines) during blowing phase is as follows. In case of the rectangular exit, the vortex pair with semicircular vortex is generated along the spanwise direction (Phase 45 °, Fig 3.8a). The vortical structure is strong towards the end of the exit due to the three-dimensional effect, which is attributed to the induced flow velocity toward the exit due to the finite length of the exit (Phase 90 °, Fig 3.8b). As the vortex size of the slot end becomes larger, the clockwise rotating flow appears from the slot end to the slot center, and this grows toward the normal direction from the wall (Phase 135 °, Fig 3.8c). The streamlines of normal direction are dominant near the jet exit, thus the jet flow is quickly subdued after suction phase (Phase 180 °, Fig 3.8d). For the circular exit, the serial vortex rings uniformly grow along the spanwise direction from phase 45 ° to phase 90 ° (Fig. 3.9a-b). As a result of the interactions with an external flow field, jet vortices develop into the downstream direction, and the clockwise rotating flow at the slot end is relatively smaller (Phase 135 °, Fig. 3.9c). For phase 180 ° (Fig. 3.9d), the vortical structure moves away from the jet exit, and effect of jet vortices is far-reaching along the streamwise distance. This is consistent with the results of the time-averaged vortical structures, which

indicates that the circular exit produces a more sustainable vortical flow compared to that of the rectangular one.

3.3.2 Flow Control Effectiveness

The variation in wall shear stress is a useful indicator of the effect on flow separation delay [65]. The smaller the decrease of the wall shear stress ratio curve, the more the flow field can preserve the jet vortical structure. From this perspective, the flow control effect of the exit configuration was evaluated by comparing the time-averaged wall shear stress distributions for two types of synthetic jets. Figure 3.10 shows wall shear stress ratio along the streamwise and the spanwise directions. The X-axis is the spanwise distance, and the Y-axis is the ratio of jet-on values (τ_{wall}) to jet-off values (τ_{w_ref}) along the streamwise distance. The streamwise locations are 5, 20, 50, 80, 120, and 200 mm from the origin, and the spanewise locations are from y = 0 mm to y = 40 mm. In case of the rectangular exit, at x = 5 mm, overall wall shear stress ratio is much higher and increases toward the end of the slot, but the values quickly decrease after x = 20 mm. Combined with the result of Fig. 3.8, this indicates that the vortex pair with the semicircular vortex favorably affects strength of initial jet vortex. However, the clockwise rotating flow caused by cross flow interaction is ineffective for transfer of initial jet momentum further downstream and makes the vortex persistency weaker. For the circular exit, the wall shear stress values are relatively preserved along the streamwise direction. The distributions are oscillatory

due to the exit configuration. The maximum values coincide with the center of the circular holes, and the minimum values are located between two adjacent holes. The peak value, which is caused by the semi-clockwise vortex of exit end, moves into the exit center along the downstream direction. From the results of flow structures, the rotating flow of exit end is smaller than that at the rectangular exit, and thus the vortical flow effect is far-reaching to the flow field. This indicates that the serial vortex rings favorably interacts with the freestream to preserve the initial vortex, so it is able to survive longer to have an effect on the flow fields.

Figure 3.11 shows the slope of the time-averaged wall shear stress ratio. This can readily indicate as a way to compare the effectiveness of flow control along the downstream direction. The small slope of the wall shear stress ratio means the preservation of the jet effect. A similar behavior can be seen more clearly over all locations. Upon comparing the values of two exits, the rectangular exit has about 50 percent reduction, while the circular exit has about 30 percent reduction in the wall shear stress distribution along the streamwise direction. Judging from the comparisons, it is observed that the circular exit is relatively more effective for separation delay since it preserves the vortex structure from the jet exit better the rectangular exit.

3.4 Characteristics of Circular Exits Depending on Hole Parameter

Numerical simulations were performed by changing the major parameters of the multiple serial circular exit: the circular hole gap (G) and the hole diameter (D) of 0.5L-2L. The reference length (L) used for the circular hole diameter is shown in Fig. 3.1. Table 3.1 presents the range of the hole parameters and the notation of each exit configuration. In order to maintain the same total jet momentum condition and span length, the total number of circular holes and the jet peak velocity are varied, as shown in Table 3.2.

3.4.1 Variation of Hole Gap

The flow characteristics were analyzed for hole gaps of 0.5L, 1L, and 2L with the same hole diameter 1L. Figure 3.12 shows the iso-vorticity surface contours of each exit at the blowing phase from 60 º to 120 º under the quiescent condition. In case of G0.5D1, an additional mixing vortical structure is created between the two single circular holes by the interaction of serial vortex rings along the spanwise direction, which leads to a greater effect of vortical structures on the spanwise flow characteristics. For G2D1, overall vortex rings of the circular exit exhibit a three-dimensional flow structure without additional mixing between two adjacent holes.

A similar behavior can be seen in the vortical structure for the cross flow condition. Figure 3.13 shows the time-averaged vorticity magnitude

contours along the spanwise distance right after the jet exit in the cross flow interaction. The vortex rings of G0.5D1 case interact greatly with adjacent ones in serial circular jets, while the jet vortices of G2D1 case have a small interaction with each other. Flow characteristic of G1D1 case have a medium between G0.5D1 case and G2D1 case in terms of the initial jet interaction.

The close-up view of flow structures at blowing peak are shown in Fig. 3.14. Since the blowing component affects the far field region, the vortex structure of the blowing phase is important for sustaining vortical flow characteristics. The flow structure at blowing peak depends on the interaction of initial jet vortex along the spanwise direction. G0.5D1 case has a large semi-clockwise rotating vortex at the end of the slot, while G2D1 case has a series of vortex rings without rotating flow at the slot end. Based on the results of the rectangular exit and the circular exit, it is observed that the clockwise rotating flow of the rectangular exit have a positive effect on the strength of initial jet vortex. Furthermore, in case of the circular exit, the additional mixing by the interaction of serial vortex rings produces a more sustainable vortical flow characteristic in the cross flow interaction. From this perspective, G1D1 case is a proper choice for relatively stronger and more sustainable vortical structure.

Figure 3.15 shows the slope of the time-averaged wall shear stress ratio depending on the hole gap. In the case of G0.5D1, the overall wall shear stress distributions are quite similar to those of the rectangular case. The flow structures of G0.5D1 negatively interact with the freestream, which makes the vortex persistency weaker and leads to a sharp decrease of the

wall shear stress ratio along the streamwise direction. For G2D1 case, the increase of the wall shear stress ratio is observed near the jet exit, which implies that the small vortex interaction is ineffective for increasing the initial vortex strength. By considering effective initial strength and persistency of jet vortices, together with all of the previous comparisons, this confirms that suitable hole gap beneficially changes the local flow feature and vortex structure for effective flow control.

3.4.2   Variation of Hole Diameter

Flow characteristics were analyzed according to the hole diameter and the hole gap of 0.5L, 1L, and 2L, as shown in Fig. 3.16. The distributions of wall shear stress ratio depending on the hole diameter are quite similar, and the gap = 1L cases display a favorable distribution for each hole diameter. This indicates that the hole gap is more dependent on flow control effectiveness than the that of the hole diameter.

Based on the comparisons, the flow control characteristics of a synthetic jet are greatly dependent on the exit configuration, and the circular exit with a suitable hole configuration provides a notably better performance than the rectangular exit with all the other parameters fixed.

Chapter IV

Active Flow Control of Wing

4.1 Experimental Reference

4.1.1 BWB Configuration

The 3-D wing configuration was modified from the Boeing/AFRL 1303 UCAV model. This BWB model was made based on the NACA 64A201 airfoil. The modifications from 1303 UCAV model were wing span length and twist angle. The mean aerodynamic chord was 1.184 m and the wing span was 2 m. The twist angle at wing tip was -5 °. Total weight of BWB configuration except for support fixture was about 100 kg. Details of BWB configuration are shown in Table 4.1. Figure 4.1 shows BWB model upper surface with synthetic jet and pressure tap locations. The leading edge of wing was instrumented with 7 modules of synthetic jet actuator, where the leading edge slot is divided into two individually addressable sections. Each module was a width of 80 mm, a length of 78 mm, a height of 8 mm, and a weight of 100g. Total weight of 7 modules is 0.7% of BWB model. Actuators were powered by two 63.5 mm piezoelectric disks. There was a break between the three inboard actuators and the four outboard actuators along the leading edge of approximately 15 mm because of structural

constrains. The model was equipped with chord-wise 8 lines of pressure taps between $\eta = 0.3$ and $\eta = 0.9$. These taps were limited to the leading edge and trailing-edge region. The pressure distributions were analyzed along chordwise direction and spanwise direction. As shown in Fig. 4.1, the X-direction is along the streamwise direction, the Y-direction is along the spanwise direction of the exit, and the Z-direction is along the normal direction from the wall. The origin of the coordinate is the apex of the wing.

In order to be lightweight and increase jet momentum, dual-diaphragm and piezoelectric actuators is used for 3-D flow control. Jet momentum is produced by the volume change of a cavity by two piezoelectric diaphragms, as shown in Fig. 4.2a. The manufactured synthetic jet module is presented in Fig. 4.2b. The performance of piezoelectric synthetic jet actuator was tested in a quiescent condition and separated-flow condition [66]. In previous Chapter, the results indicate that the circular exit configuration with a suitable hole configuration is effective for active flow control experiments. Therefore, the exit configuration of actuator was circular exit having 17 circular holes of a hole diameter of 1.5 mm, a hole gap of 1.5 mm.

4.1.2   Experimental Setup

Experimental tests were conducted in the KARI (Korea Aerospace Research Institute) subsonic wind tunnel, as shown in Fig. 4.3. The working section is 4 m wide x 3 m high x 5 m long. The baseline and active flow

control enhanced aerodynamic performance of the full-scale BWB model (Fig. 4.4), were measured in wind-tunnel testing. Static pressure was obtained using a net pressure scanner. Forces and moments were acquired via an external six-component balance. In order to perform the surface flow visualization, tufts were installed on the upper surface along the streamwise direction. For uncontrolled case, model configuration was tested at angles of incidence, from 0 ° to 20 ° at zero sideslip for force and pressure measurements. For controlled case, synthetic jet modules near the leading edge were operated in the post-stall regime to examine the flow control performance of a synthetic jet.

The mean chord Reynolds number was 9.6×10^5 with freestream velocity of 20 m/s. In the controlled case, synthetic jet actuators were operated at 40 m/s peak velocity with a frequency of 200 Hz.

4.2   Baseline Analysis

4.2.1   Code Validation

The Reynolds number based on mean aerodynamic chord is from of the mean chord length is 9.4×10^5, the freestream velocity is 20 m/s. Turbulence model used in the present computation is the Menter's SST-DES model to provide excellent predictions of flow separation.

The 3-D body conforming C-H type of grid is generated around BWB configuration by using commercial software GridgenV15. The grids

are clustered properly near the leading and trailing edges and the tip, where the flow is expected to undergo rapid changes. The grid is nearly orthogonal at the surface, with the first grid line lying at 0.00001c normal to the wing surface and 146 and 194 are chosen in the chordwise and spanwise directions respectively. The outer grid boundary is located at 25 chords from the wing surface. The geometric growth rate does not exceed 1.05 in any direction, and the resulting z+ values range from 1 in areas of separated flow, to over 3 in reattachment regions, to 5 at the leading edge. The 3-D volume grid is plotted in Fig. 4.5a to illustrate the grid topology, while the grid clustering near and on the surface of the wing is shown in Fig. 4.5b.

Verification study has been performed in term of grid refinement with five angles of attack (0 º, 5 º, 10 º, 16 º, and 20 º). Figure 4.6 shows the comparison of computed aerodynamic coefficients with experimental data. After preliminary computations on a very coarse grid consisting of approximately 3.1 million cells and spanning a large computational domain, the clustering near the wing surface has been modified and the extent of the domain has been significantly reduced. To examine the grid sensitivity, three grid densities were considered for the control-off case. From the comparison of the computed results, computational differences between fine mesh and medium mesh are less than 2%, which is thought to be adequate for reliable computations. Thus, mesh systems of 6.1 million grid points was considered for the control-off case. Using the determined grid systems, steady and unsteady flow calculations were performed depending on the range of angle of attack. The results were obtained to have converged when the integrated

force coefficient were stable. For unsteady computations, sub-iteration in pseudo-time was conducted until the maximum flow divergence of a converged solution at the fixed physical time was less than 1.0×10^{-5} to maintain sufficient temporal accuracy. The results of the uncontrolled BWB configuration were compared with the experimental data overall angles of attack. Though there are some differences between computational prediction and experimental measurement, overall comparison indicates that computed results capture accurately enough to understand the main flow physics.

4.2.2   Flow Characteristics of BWB Configuration

In order to understand the developing flow topology with increasing angle of attack, flow features of the uncontrolled cases were analyzed by both experimental and numerical methods.

To examine the flow structure and characteristics, surface pressure coefficient distributions were analyzed by both experimental and numerical results over the range 8 º≤ angle of attack ≤16 º in 2 º increments, as shown Fig. 4.7. Left figures are based on interpolation data of experimental sectional pressure coefficient, which indicate the qualitative flow features on the wing surface. Right figures are computed surface pressure coefficient contours. As shown in Fig 4.6, the stall angle is about 10 º in the aerodynamic coefficient curves. The computed results agree fairly well with the experimental data except near the region of stall. From the experimental and numerical results, the general behavior near the post-stall region is

captured accurately enough to understand the main characteristics of flow physics.

At angle of attack of 8 º (Fig. 4.7a), leading edge vortex core is shown as a stable low-pressure region. At angle of attack of 10 º (Fig. 4.7b), the suction area appears along the leading edge, which means that the leading edge vortex is developed on the upper surface. The small separation flow is also observed near the wing tip of the wing. At angle of attack of 12 º (Fig. 4.7c), leading edge vortex breakdown is shown in the inboard section of the wing. When vortex breakdown take place, the vortex core suddenly is expanded and the flow separation of outboard region is accelerated. At angle of attack of 14 º (Fig. 4.7d), the large separation region appears on the outboard region. As a result, the vortex breakdown region and separated-flow region are merged into each other, and the multiple patterns of separation present on the wing surface. At angle of attack of 16 º (Fig. 4.7e), the size of the suction area becomes larger in the inboard region and the separated flows expand from the outboard section to the inboard section.

Figure 4.8 shows iso-vorticity contour colored pressure coefficient. The vorticity contours present the tendency of flow structure with increasing angle of attack. The leading edge vortex core develops from the aft of leading edge and flow separation starts from outboard region of the wing as angle of attack increases. Through an analysis of computed flowfields, it is observed that both the leading edge vortex breakdown in the inboard section and the flow separation in the outboard section are critical in determining the aerodynamic performance.

4.3   Flow Control of BWB Configuration

The objective of the first part is to understand flow control mechanism depending on jet location based on the baseline flow feature. In the second part, flow control strategy of low speed fight is applied for flow control of high speed flight.

4.3.1   Flow Control Depending on Jet Location

In order to examine the overall flow control performance in the post-stall region, all synthetic jet modules near the leading edge were operated from angle of attack of 10 º to angle of attack of 20 º in 1 º increments. Figure 4.9 shows the increment of lift to drag ratio versus angle of attack in the post-stall region. Synthetic jets affect the flow control of BWB configuration for all angles of attack, and the improvement of aerodynamic coefficients is most visible near the stall angle.

Although the all-actuators-on case affects the flow control and the lift to drag ratio enhancement, it causes large weight and power of the synthetic jet, which may not effective against an efficient design and low power supply. Thus, to investigate an effective flow control strategy, which means high performance and low power, the flow control experiments were performed by changing the number of synthetic jet modules. Angle of attack is fixed at angle of attack of 12 º, which is the maximum enhancement in lift to drag ratio.

Figure 4.10 shows total increment and increment per module of lift to drag ratio depending on the number of synthetic jet modules. The increment of lift to drag ratio per module refers to flow control efficiency. When operating synthetic jet module increases, overall control performance increases and control efficiency decreases. The change tendency is similar depending on the number of jet modules. Cases including #6#7 jets and #1#2 jets represent more effective results in operating conditions of two, three, and four jets on.

Since the actual flow control mechanism and flow structure can be fundamentally different between #6#7 jets-on case (inboard jets) and #1#2 jets-on case (outboard jets), numerical simulation was conducted depending on the jet location. To test the grid sensitivity, three sets of grids with increasing grid densities were considered for each case. From the comparisons of the computed results in Fig. 4.11, 17 million grid points was chosen in selective-actuators-on case.

Figure 4.12 shows time-averaged iso-surface vorticity colored pressure coefficient of the two cases. The inboard jets favorably interact to delay the leading edge vortex breakdown, and thus, it is able to extend the leading edge vortex and make stable flow near the jets. The outboard jets suppress the formation of the flow separation in the outboard region. The vortices produced by the outboard jets continuously disturb the large separation vortex, which leads to substantial reduction of separated flow.

In order to compare the flow control characteristics depending on the jet location, the time-averaged surface pressure coefficient contours were

examined, as shown in Fig. 4.13. For inboard jets, synthetic jets are located in developing leading edge vortex. By operating inboard jets, the starting point of leading edge vortex breakdown is moved toward the outboard section and jets also affect outboard flow region. For outboard jets, synthetic jets are located in the separated flow region. Synthetic jets affect the outboard flow feature and reduce the separation region. In both cases, a more stable flow structure is developed on the suction surface. The change of local flow pattern and decrease of suction area on the upper surface are also observed experimentally in pressure coefficient contours based on the interpolation data.

Figures 4.14 and 4.15 are time-averaged pressure coefficient contours compared with the uncontrolled case from $\eta = 0.6$ to $\eta = 0.9$. The axis is a normalized value of the length divided by the reference length, which is a half-span of the wing. Flow control mechanism depending on the jet location can be clearly observed. For inboard jets, jet location is about form $\eta = 0.4$ to $\eta = 0.5$. The starting point of vortex breakdown is moved toward the outboard section from $\eta = 0.65$ to $\eta = 0.75$. They also provide a stable flow structure in the outboard region. The outboard jets, which is located in about from $\eta = 0.7$ to $\eta = 0.8$, make the leading edge vortex strength stronger at $\eta = 0.6$ and decrease the size of flow separation at each section from $\eta = 0.7$ to $\eta = 0.9$. This confirms that the inboard jets provide delay of leading edge vortex breakdown, while the outboard jets affect separation control.

Judging from the comparisons, it is observed that selective-actuators-on case based on the baseline flow characteristics is effective for changing the local flow feature and vortex structure to bring a significant improvement of the wing aerodynamics acting on BWB configuration in the stall angle.

4.3.2   Application of Flow Control in High Speed Flight

Based on baseline analysis according to freestream velocity, selective-actuators-on strategy of low speed flight is applied to flow control of high speed flight. Figure 4.16 shows aerodynamic coefficient according to freestream velocity by wind tunnel test. When the freestream velocity increases, lift increases and drag decreases at the same angle of attack. Because of BWB configuration, aerodynamic performance is enhanced at high speed flight.

In order to understand the developing flow topology with increasing angle of attack in high speed flight, flow features of the uncontrolled cases were analyzed. The Reynolds number based on mean aerodynamic chord is from of the mean chord length is 3.8×10^6, the freestream velocity is 80 m/s. Mesh systems of 6.1 million grid points, which was the results of grid sensitivity test in freestream velocity of 20 m/s, was considered. Baseline analysis in high speed flight was performed over the range 10 º$\leq$ angle of attack $\leq$18 º in 2 º increments. Figure 4.17 shows the comparison of computed aerodynamic coefficients with experimental data. The results of

the uncontrolled BWB configuration were compared with the experimental data overall angles of attack in high speed flight.

To examine the flow structure and characteristics at freestream velocity of 80 m/s, surface pressure coefficient distributions were analyzed, as shown Fig. 4.18. Flow patterns of high speed flight are similar to flow characteristics of low speed flight with increasing angle of attack. However, compared to freestream velocity of 20 m/s, the starting point of leading edge vortex breakdown is shown toward outboard section and unstable flow structure of outboard region is smaller in overall angle of attack. From this perspective, flow control strategy of low speed flight is applicable to flow control of high speed flight at the same control angle of attack of 12 °.

Inboard jets (#6#7 jets) and outboard jets (#1#2 jets) are conducted for flow control of high speed flight under the same mesh system (17 million grid points). Figure 4.19 shows time-averaged iso-surface vorticity colored pressure coefficient of the two cases. Because both of them are located in developing leading edge vortex, they affect delay of leading edge vortex breakdown and flow structure of outboard region. The strength of leading edge vortex is stronger and unstable flow region is effectively decreased in outboard region. From the numerical results in high speed flight, lift to drag ratio is increased about 16 percent, respectively.

Figure 4.20 is time-averaged pressure coefficient contours compared with the uncontrolled case. From $\eta = 0.75$ to $\eta = 0.9$, synthetic jets decrease the size of flow separation at each section. Judging from the comparisons, it is observed that flow control strategy of low speed is effectively applicable

to flow control of high speed, and stall characteristics and control performance are remarkably improved in overall flight speed condition.

.

Conclusion

To bring an improvement of the wing aerodynamics acting on the three-dimensional aircraft configuration, flow characteristics of synthetic jets depending on exit configuration were analyzed, and flow control using synthetic jets was then conducted over BWB configuration.

Flow characteristics of synthetic jets were numerically investigated for different exit configurations under a cross flow condition. For the rectangular exit, the vortex pair with the semicircular vortex negatively interacts with the freestream, which makes the vortex persistency weaker further downstream. In case of the circular exit, the serial vortex rings are uniformly developed into the streamwise direction, and the vortical structure favorably interacts to maintain the strength of the initial vortex. Thus, the circular exit is able to affect much wider flow region than the rectangular one. Comparative studies were then conducted according to the hole gap and the hole diameter of circular exit with all the other parameters fixed. Detailed numerical simulations suggest that the hole gap has much more significant effect on flow control than hole diameter. Based on the comparisons, regardless of hole diameter, the circular exit with a proper hole gap produces desirable interactions between jet vortices and freestream, which leads to a stronger and relatively more sustainable vortical structure.

The 3-D wing configuration was BWB configuration modified from the 1303 UCAV model. The leading edge of wing was instrumented with

synthetic jet actuators, which have designed circular exit. Flow features of the uncontrolled and controlled cases were analyzed by both experimental and numerical methods. For uncontrolled case, the leading edge vortex breakdown develops from inboard region and flow separation starts from outboard region of the wing as angle of attack increases. In order to investigate an effective flow control strategy, selective-actuators-on case was examined in terms of high performance and low power. For inboard jets, jet vortices are able to extend the leading edge vortex, and favorably interact to delay the leading edge vortex breakdown along spanwise direction. For outboard jets, jet vortices continuously affect the outboard flow feature, which leads to substantial decrease the size of flow separation. Based on the baseline analysis according to freestream velocity, flow control strategy of low speed flight is applied for flow control of high speed flight. Consequently, synthetic jets change the global flow-field structure effectively, and stall characteristics and control performance are remarkably improved in overall flight speed condition.

Judging from the results, it is observed that the synthetic jet under suitable operating conditions beneficially changes the local flow feature and vortex structure to bring a significant improvement of the wing aerodynamics acting on the three-dimensional aircraft configuration in the stall angle.

References

[1] M. Amitay, D. R. Smith, V. Kibens, D. E. Parekh, A. Glezer, Aerodynamic flow control over an unconventional airfoil using synthetic jet actuators, AIAA Journal 39 (3) (2001) 361-370

[2] L. W. Traub, A. Miller, O. Rediniotis, Effects of synthetic jet actuation on a ramping NACA 0015 airfoil, Journal of Aircraft 41 (5) (2004) 1153-1162

[3] H. Wang, S. Menon, Fuel-air mixing enhancement by synthetic microjets, AIAA Journal 39 (12) (2001) 2308-2319

[4] A. Pavlova, M. Amitay, Electronic cooling using synthetic jet impingement, Journal of Heat Transfer 128 (2006) 897-907

[5] D. Greenblatt, I. Wygnanski, The control of separation by periodic excitation, Progress in Aerospace Science 36 (7) (2000) 487-545

[6] A. Crook, N. J. Woodf, Measurements and visualizations of synthetic jets, in: 39th Aerospace Sciences Meeting and Exhibit, AIAA 2001-0145, Reno, Nevada, January 2001

[7] Li-Hao Feng, Jin-Jun Wang, Particle image velocimetry study of parameter influence for synthetic-jet application, Flow Measurement and Instrumentation 34 (2013) 53-67

[8] Li-Hao Feng, Jin-Jun Wang, Modification of a circular cylinder wake with synthetic jet: Vortex shedding modes and mechanism, European Journal of Mechanics - B/Fluids 43 (2014) 14-32

[9] F. Cannelle, M. Amitay, Transitory behavior of a finite span synthetic jet, Physics of Fluids 19 (9) (2007)

[10] M. Amitay, F. Cannelle, Evolution of finite span synthetic jets, Physics of Fluids 18 (5) (2006)

[11] B.R.Ravi, R. Mittal, F.M. Najjar, Study of three-dimensional synthetic jet flowfields using direct numerical simulation, in: 42nd AIAA Aerospace Sciences Meeting and Exhibit, AIAA 2004-0091, Reno, NV, January 2004

[12] C.L. Rumsey, N.W. Schaeffler, I.M. Milanovic, K.B.M.Q. Zaman, Time-accurate computations of isolated circular synthetic jets in crossflow, Computers & Fluids 36 (6) (2007) 1092-1105

[13] B. Gunther, Frank Thiele, R. Petz, W. Nitsche, J. Sahner, T. Weinkaufk, H.-C. Hege, Control of separation on the flap of a three-element high-lift configuration, in: 45th AIAA Aerospace Sciences Meeting and Exhibit, AIAA 2007-265, Reno, Nevada, January 2007

[14] R. Petz, W. Nitsche, Active separation control on the flap of a two-dimensional generic high-lift configuration, Journal of Aircraft 44 (3) (2007) 865-874

[15] S. H. Kim, C. Kim, Separation control on NACA23012 using synthetic jet, Aerospace Science and Technology 13 (2009) 172-182

[16] M. Kim, S. H. Kim, W. Kim, Y. Kim, C. Kim, Flow control of tilt-rotor airfoils using synthetic jets, Journal of Aircraft 48 (3) (2011) 1045-1057

[17] S. Zhang, S. Zhong, Experimental investigation of flow separation control using an array of synthetic jets, AIAA Journal 48 (3) (2010) 611-623.

[18] J. L. Gilarranz, L. W. Traub, O. K. Rediniotis, A new class of synthetic

jet actuators-Part I: Application to flow separation control, Journal of Fluids Engineering 127 (2005) 367-376

[19]   A. S. Yang, J. J. Ro, M. T. Yang, W. H. Chang, Investigation of piezoelectrically generated synthetic jet flow, Journal of Visualization 12 (1) (2009) 9-16

[20]   Amitay, M., et al., Aerodynamic flow control over an unconventional airfoil using synthetic jet actuators, AIAA Journal 39 (3) (2001) 361-370

[21]   Crook, A., A.M. Sadri, and N.J. Wood, Development and implementation of synthetic jets for the control of separated flow, AIAA-1999-3176

[22]   Mane, P., K. Mossi, and R. Bryant, Experimental design and analysis for piezoelectric circular actuators in flow control applications, Smart Materials & Structures 17 (1) (2008)

[23]   Smith, B.L. and A. Glezer, The formation and evolution of synthetic jets, Physics of Fluids (10) (1998) 2281

[24]   Gallas, Q., Optimization of synthetic jet actuators, Defense Technical Information Center, 2003

[25]   Mossi, K. and R. Bryant, Piezoelectric actuators for synthetic jet applications, MRS Proceedings, Cambridge Univ Press (2003)

[26]   Mossi, K. and R. Bryant, Pre-stressed circular actuators, Ceramic Transactions (2003) 445-454

[27]   Mossi, K., et al., Boundary condition effects on piezo-synthetic jets, Integrated Ferroelectrics 71 (1) (2005) 257-266

[28]   Stephen McParlin el al., Low speed wind tunnel tests on the 1303

UCAV concept, 24th AIAA Applied Aerodynamics Conference, 2006

[29] Furlong G. C. and McHugh J. G., A summary and analysis of the low-speed longitudinal characteristics of swept wings at high Reynolds number, NACA Report 1339 (1952)

[30] Parker N. T. and Pitman R. N., Aerodynamic studies of control surfaces on a 40° lambda wing configuration (M2362), DRA/AS/LBA/CR96070/1 (1996)

[31] Parker N. T. and Ayres J. C., Mach and Reynolds number effects on a 40° lambda planform half-wing model (M2389), phase 1 tests, DERA/AS/ASD/CR97076/1 (1997)

[32] Billman, G. M., and Osborne, B. A., High L=D extended range/payload fighter aircraft technology, U.S. Air Force Research Lab., AFRL-VA-WP-TR-1999-3084, Air Vehicles Directorate (1998)

[33] Bruce, R. J., Low speed wind tunnel tests on the 1303 UCAV concept, QinetiQ, Ltd., TR 025502 (2003)

[34] McParlin, S. C. et al., Low speed wind tunnel tests on the 1303 UCAV concept, QinetiQ, Ltd., TR QinetiQ/fST/tR025502/1.0 (2003)

[35] Ghee, T. A., Parametric evaluation of deployable serrated flaps on a representative UCAV configuration, AIAA Paper 2003-3982 (2003)

[36] Ghee, T. A., and Hall, D. R., Experimental and numerical investigation of vortex shedding of a representative UCAV configuration for vortex flow control, RTO AVT Symposium, TR RTO-MP-069(I), Loen, Norway, May 2001

[37] Ol, M. V., Water tunnel velocimetry results for the 1303 UCAV configuration, AIAA Paper 2006-2990 (2006)

[38] Nelson, R. et al., Modification of the flow structure over a UAV wing for roll control, AIAA Paper 2007-0884 (2007)

[39] Kosoglu, M., Flow structure along a 1303 Unmanned Combat Air Vehicle, Ph.D. Thesis, Lehigh University, Bethlehem, PA (2007)

[40] Wong, M. D., and Flores, J., Application of OVERFLOW-MLP to the analysis of the 1303 UCAV, AIAA Paper 2006-2987 (2006)

[41] Zhang, F., Khalid, M., and Ball, N., A CFD based study of UCAV 1303 model, AIAA Paper 2006-4615 (2005)

[42] Petterson, K., CFD analysis of the low-speed aerodynamic characteristics of a UCAV, AIAA Paper 2006-1259 (2006)

[43] Mehul P. Patel et al., Plasma actuators for hingeless aerodynamic control of an unmanned air vehicle, Journal of Aircraft 44 (4) (2007) 1264-1274

[44] M. Amitay et al., Active Flow control on the stingray uninhabited air vehicle: transient behavior, AIAA Journal 42 (11) (2004) 2205-2215

[45] James J. Chung et al., Numerical investigation of UCAV 1303 configuration with and without simple deployable vortex flaps, 24th Applied Aerodynamics Conference, San Francisco, California, 2006

[46] M. Atkinson and F. Ferguson, A computational fluid dynamics investigation of the 1303 UCAV configuration with deployable rao vortex flaps, 44th AIAA Aerospace Sciences Meeting and Exhibit, Reno, Nevada, 2006

[47] J. Chung et al., Landing pitch control analysis for a blended wing body UCAV, 48th AIAA Aerospace Sciences Meeting Including the New Horizons Forum and Aerospace Exposition, Orlando, Florida,

2010

[48] J. Coppin, N. Qin, T. Birch, Adjoint based aerodynamic optimisation of a UCAV, 51st AIAA Aerospace Sciences Meeting including the New Horizons Forum and Aerospace Exposition, Grapevine, Texas, 2013

[49] Wilcox, D. C., Turbulence Modeling for CFD, DCW Industries, Inc., 5354 Palm Drive, La Canada, CA, 1993

[50] Wilcox, D. C., Formulation of the k-omega turbulence model revisited, AIAA Journal 46 (11) (2008) 2823-2838

[51] Menter, F. R., Two-equation eddy-viscosity turbulence models for engineering applications, AIAA Journal 32 (8) (1994) 1598-1605

[52] Menter, F. R., Kuntz, M., and Langtry, R., Ten years of industrial experience with the SST turbulence model, Turbulence, Heat and Mass Transfer 4 (2003) 625-632

[53] M. Strelets, Detached eddy simulation of massively separated flow, AIAA 2001-0879

[54] A. J. Chorin, Numerical solution of the Navier-Stokes equations, Mathematics of Computation 22 (1968) 745-762

[55] M. M. Rai, S. R. Chakravarthy, An implicit form of the Osher upwind scheme, AIAA Journal 24 (5) (1986) 735-743

[56] K. H. Kim and C. Kim, Accurate, efficient and monotonic numerical methods for multi-dimensional compressible flows Part I: Spatial discretization, Journal of Computational Physics 208 (2005) 527-569

[57] A. Travin, M. Shur, M. Strelets, P. R. Spalart, Physical and numerical upgrades in the Detached-Eddy Simulation of complex turbulent flows,

Fluid Mechanics and Its Applications 65 (2002) 239-254

[58] F. R. Menter, Assessment of higher order turbulence models for complex two- and three-dimensional flowfileds, NASA-TM-103944 (1992)

[59] K. H. Kim and C. Kim, Accurate, efficient and monotonic numerical methods for multi-dimensional compressible flows Part II: Multi-dimensional limiting process, Journal of Computational Physics 208 (2) (2005) 570-615

[60] S. Yoon, D. Kwak, Three-dimensional incompressible Navier-Stokes solver using Lower-Upper Symmetric Gauss-Seidel algorithm, AIAA Journal 29 (6) (1991) 874-875

[61] C. L. Rumsey, T. B. Gatski, W. L. Seller III, V. N. Vasta, S. A. Viken, Summary of the 2004 CFD validation workshop on synthetic jets and turbulent separation control, AIAA-2004-2217 (2004)

[62] H. Ok, Development of an incompressible Navier-Stokes solver and its application to the calculation of separated flows, Ph. D. Dissertation, Dep't of Aeronautics and Astronautics Eng., Univ. of Washington (1993)

[63] L. D. Kral, J. F. Donovan, A. B. Cain, A. W. Cary, Numerical simulation of synthetic jet actuators, AIAA paper 97-1824 (1997)

[64] W. Kim, C. Kim, K. J. Jung, Separation control characteristics of synthetic jets depending on exit configuration, AIAA Journal 50 (3) (2012) 559-570

[65] J. Zhou, S. Zhong, Numerical simulation of the interaction of a circular synthetic jet with a boundary layer, Computers & Fluids 38

(2) (2009) 393-405

[66] Byunghyun Lee, Experimental study on active flow control of synthetic jet in stalled condition, Ph.D. Thesis, Seoul National University, Korea (2014)

Table 3.1   Notation of the hole parameters

Diameter \ Gap	0.5L	1L	2L
0.5L	G0.5D0.5	G1D0.5	G2D0.5
1L	G0.5D1	G1D1	G2D1
2L	G0.5D2	G1D2	G2D2

Table 3.2   Circular hole configurations and operating conditions

Hole configuration	Total number of circular hole	Jet peak velocity (m/s)
G1D1	17	U_{peak}
G0.5D0.5	22	1.43 U_{peak}
G0.5D1	12	0.88 U_{peak}
G0.5D2	33	0.57 U_{peak}
G1D0.5	13	1.76 U_{peak}
G1D2	22	0.62 U_{peak}
G2D0.5	14	2.20 U_{peak}
G2D1	11	1.19 U_{peak}
G2D2	8	0.73 U_{peak}

Table 4.1   Specifications of BWB configuration

Span	2 m
Center chord length	1.184 m
Mean aerodynamic chord	0.708 m
Leading edge sweep	47 degree
Trailing edge sweep	30 degree
Twist angle	-5 degree (down)
Moment reference point (at 35% in wing plane)	0.602 m
Moment reference z-location	-0.033 m (aft of apex)
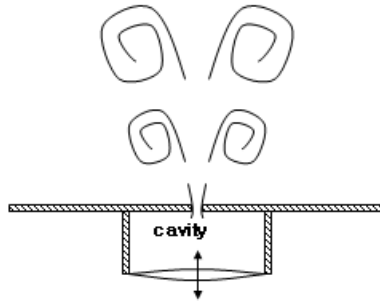
Figure 1.1   Schematic of the synthetic jet

a) Bimorph

b) Thunder

c) Lipca
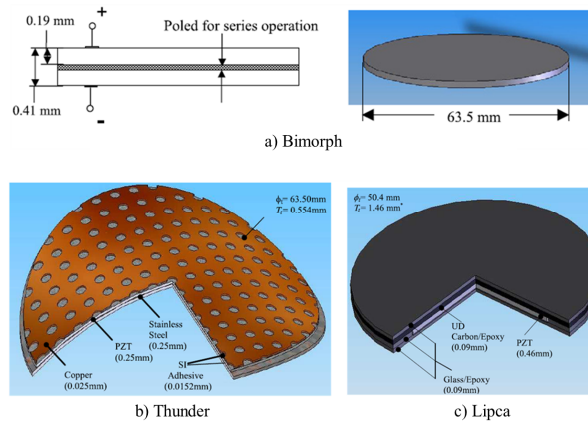
Figure 1.2   Types of piezoelectric disk
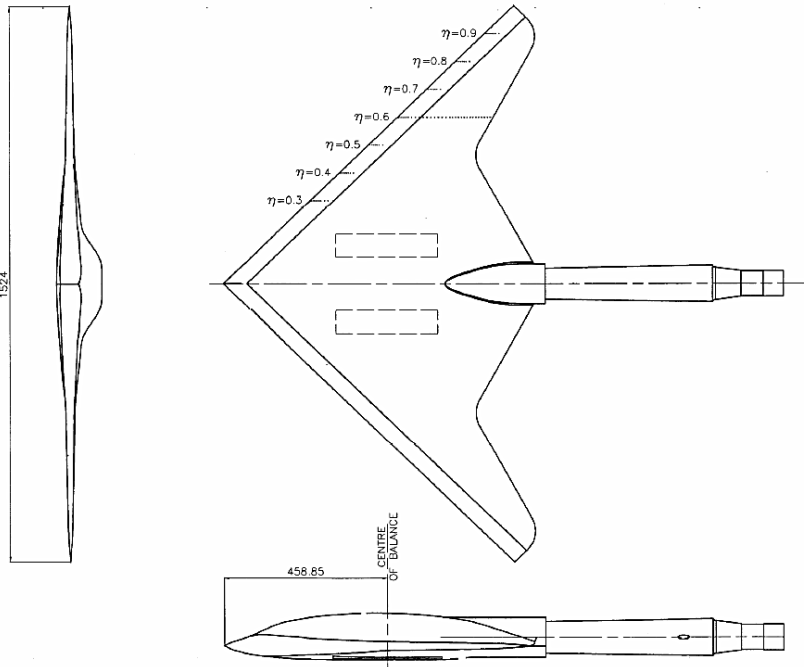
Figure 1.3   Three-view of 1303 UCAV wind tunnel model
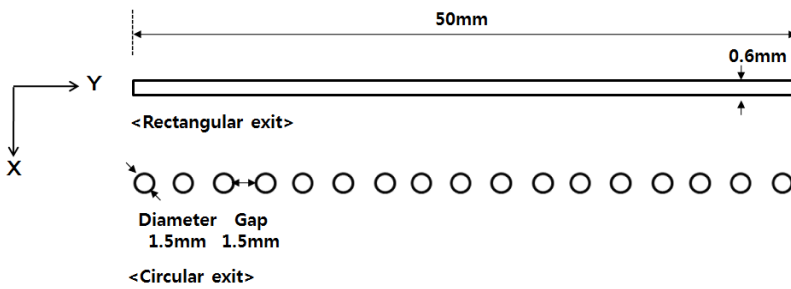
Figure 3.1   Exit configurations of the rectangular and circular exits
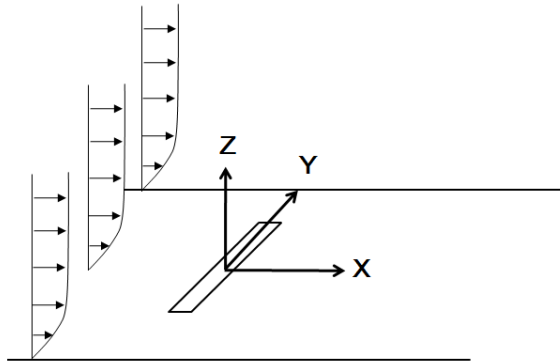
Figure 3.2   Computational coordinate system
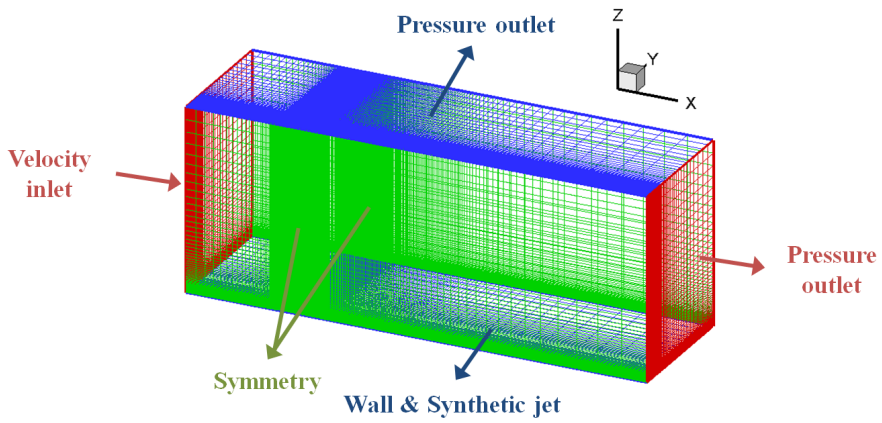
Figure 3.3   Mesh and boundary conditions
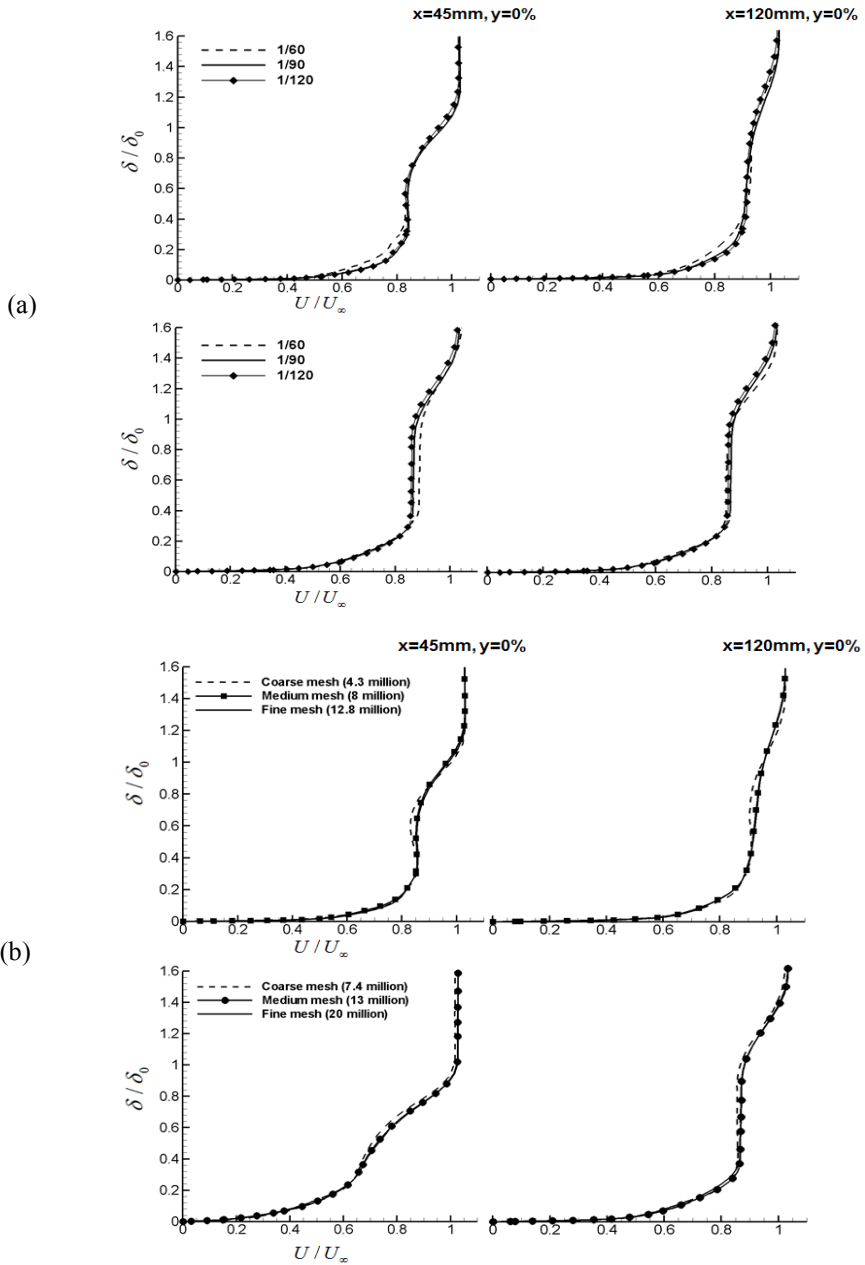
Figure 3.4   Comparison of velocity profiles

(a) computational grids; (b) time steps

(top: rectangular exit, bottom: circular exit)

90
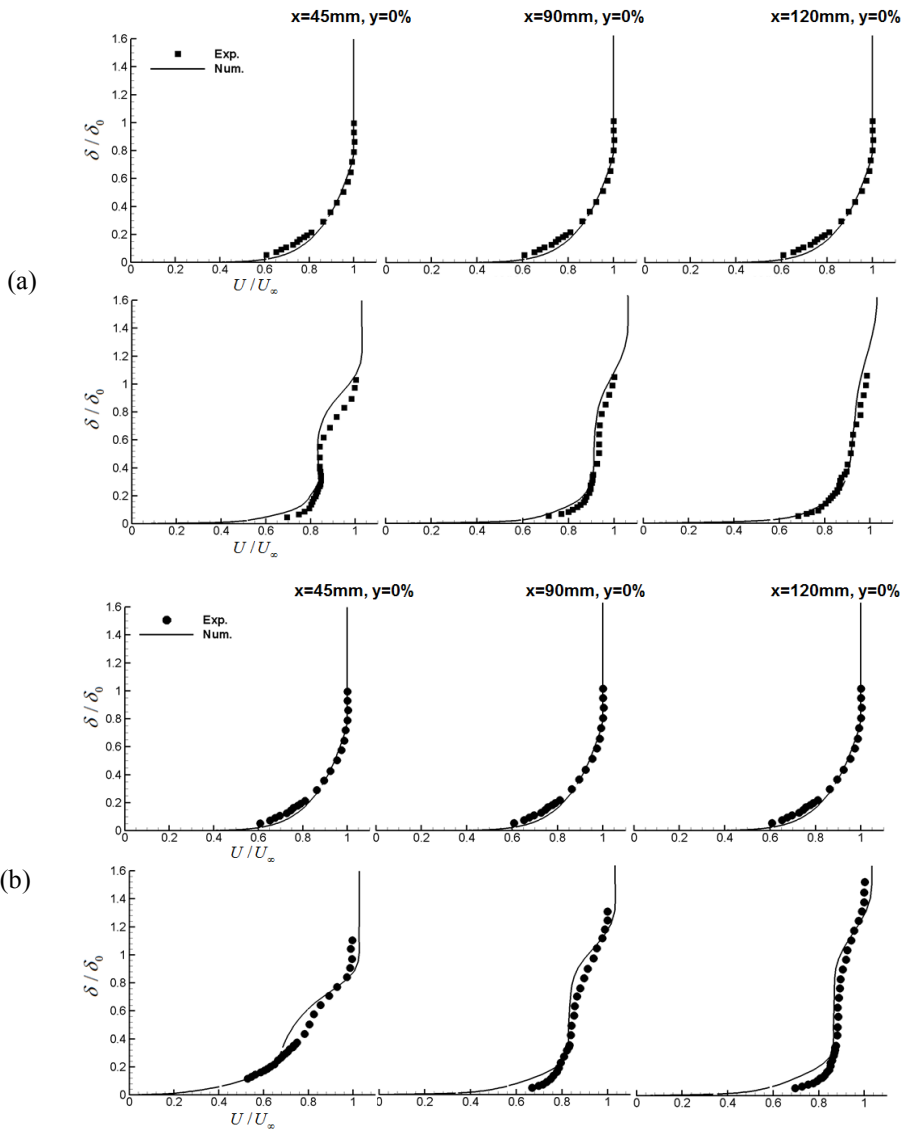
Figure 3.5   Comparison of centerline velocity profiles

(a) rectangular exit; (b) circular exit

(top: control off, bottom: control on)
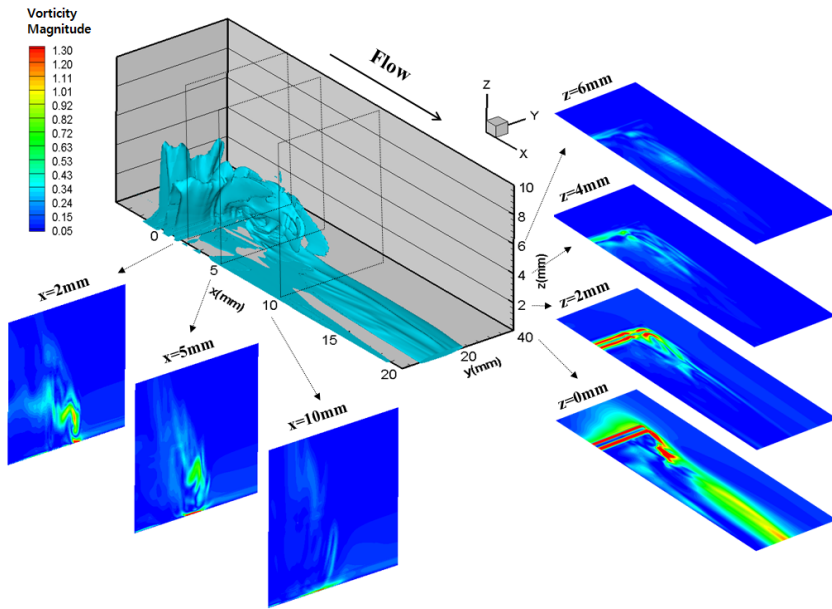
Figure 3.6   Time-averaged vortical structures of the rectangular exit
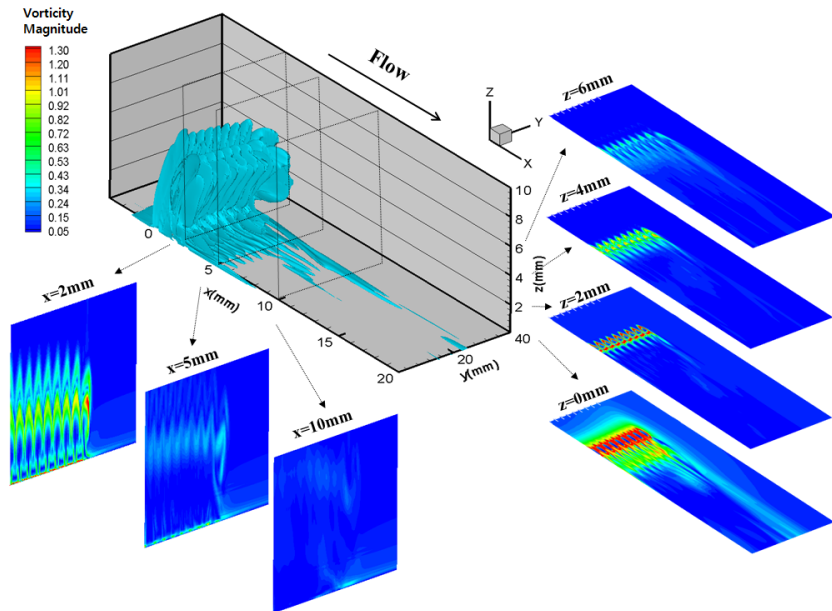
Figure 3.7   Time-averaged vortical structures of the circular exit

(a)   Phase 45 °

(b)   Phase 90 °

(c)   Phase 135 °

(d)   Phase 180 °

(e)   Phase 225 °

(f)   Phase 270 °

(g)   Phase 315 °
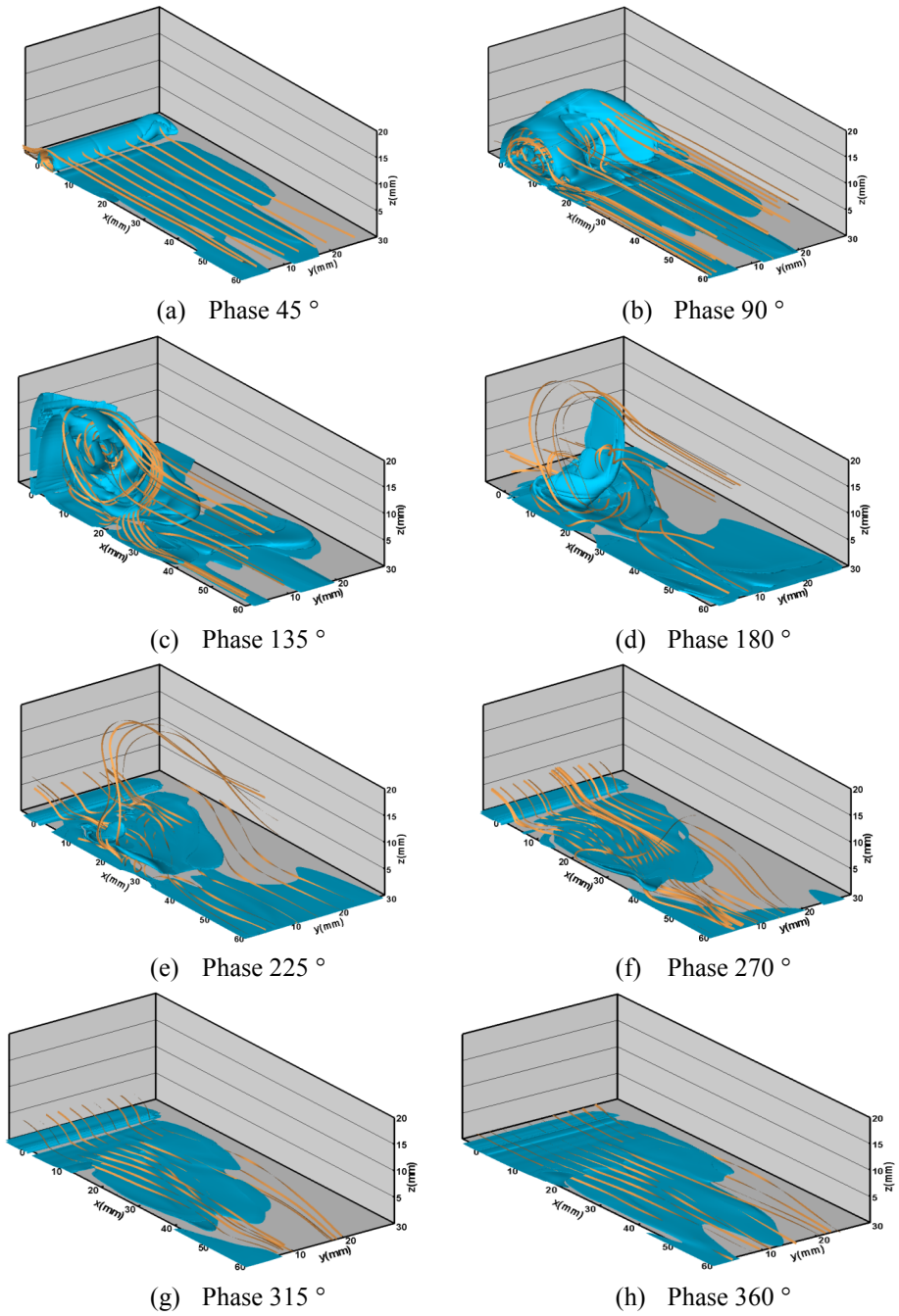
(h)   Phase 360 °

Figure 3.8   Time sequences of flow structures of the rectangular exit
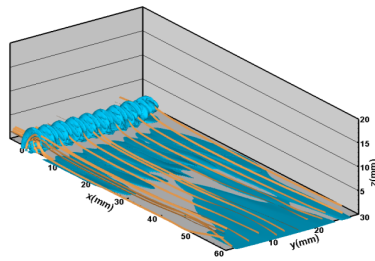
(a)　Phase 45 °
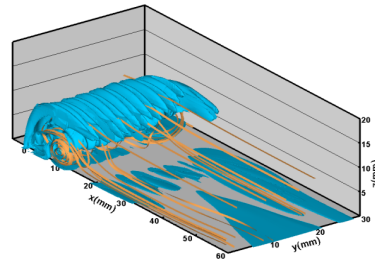
(b)　Phase 90 °
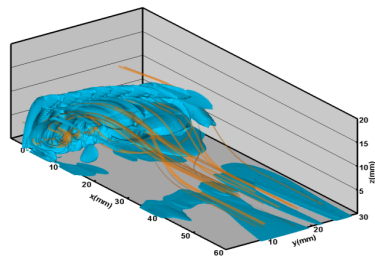
(c)　Phase 135 °
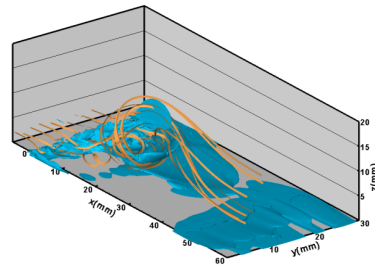
(d)　Phase 180 °
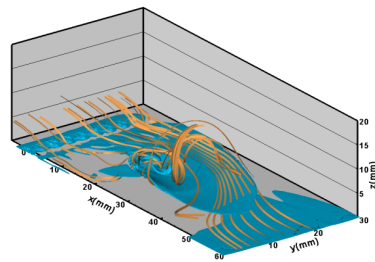
(e)　Phase 225 °
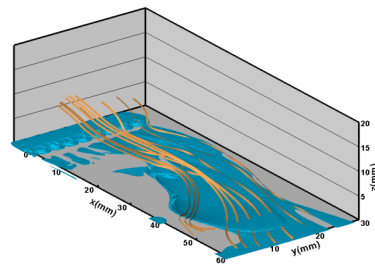
(f)　Phase 270 °
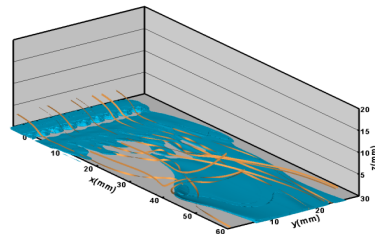
(g)　Phase 315 °
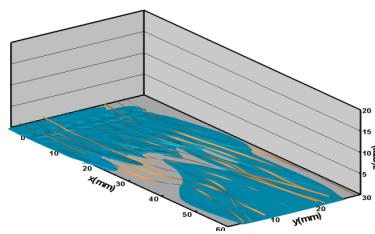
(h)　Phase 360 °

Figure 3.9　Time sequences of flow structures of the circular exit
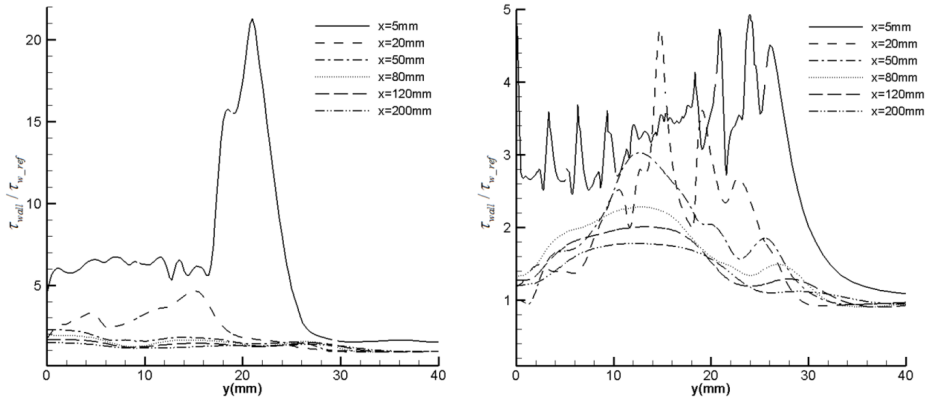
(a) rectangular exit   (b) circular exit

Figure 3.10   Time-averaged distributions of wall shear stress

(a) rectangular exit; (b) circular exit
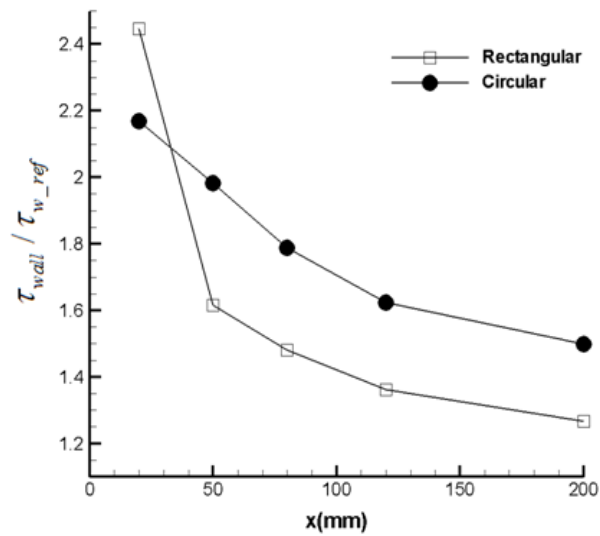
Figure 3.11   Time-averaged streamwise distributions of wall shear stress

(rectangular exit vs. circular exit)

	(a) G0.5D1	(b) G2D1
Phase 60 °		
Phase 90 °		
Phase 120 °		
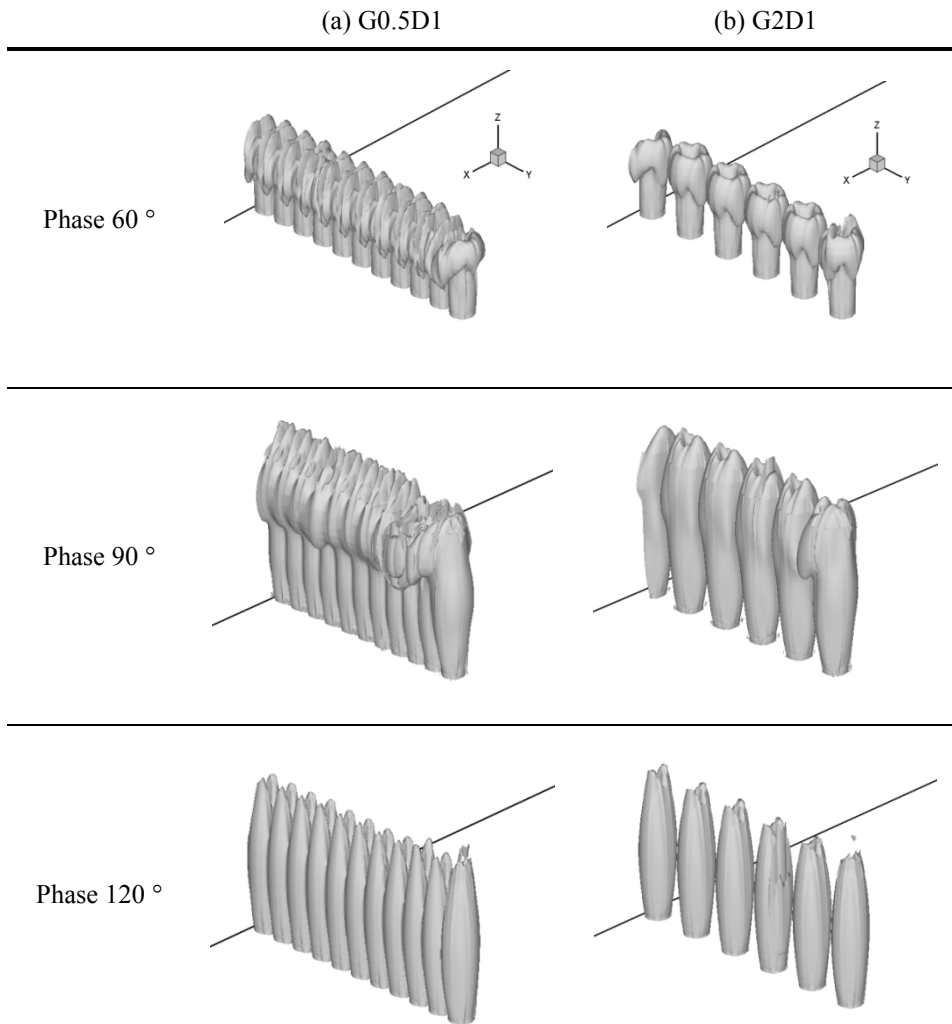
Figure 3.12   Iso-vorticity surface contours in quiescent condition;
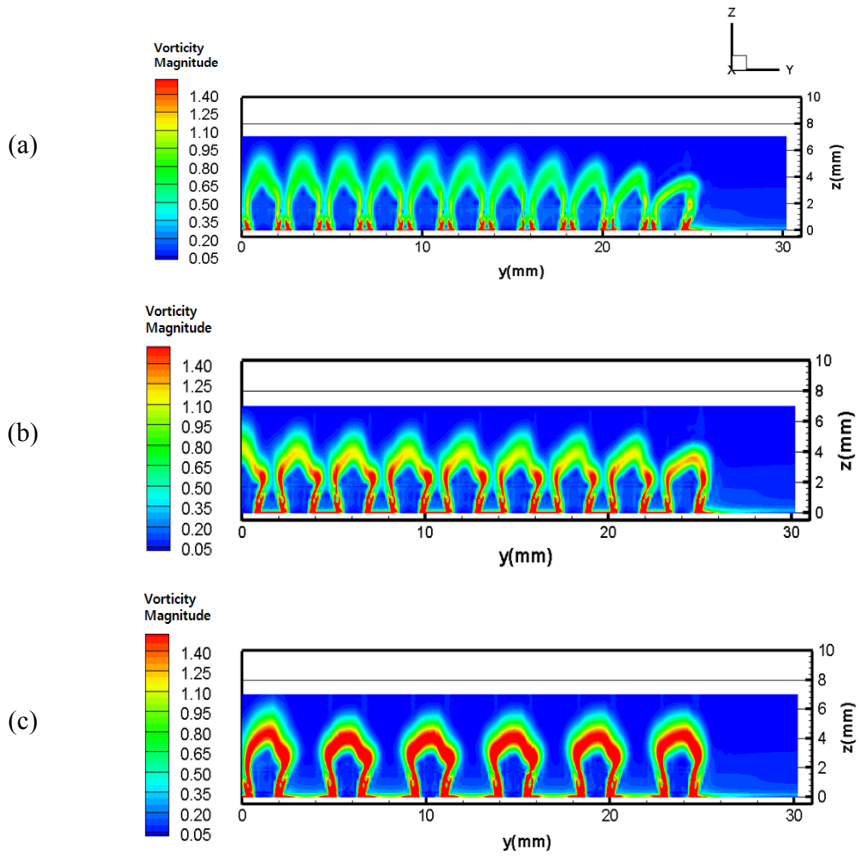
Figure 3.13   **Time-averaged vorticity magnitude contours at x = 2 mm**

(a) G0.5D1; (b) G1D1; (c) G2D1
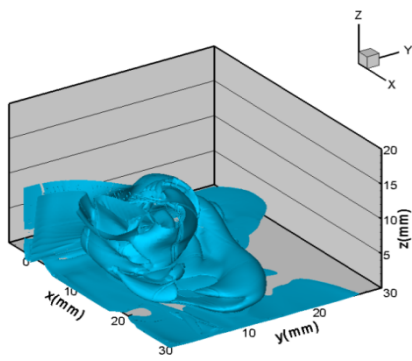
(a) rectangular exit
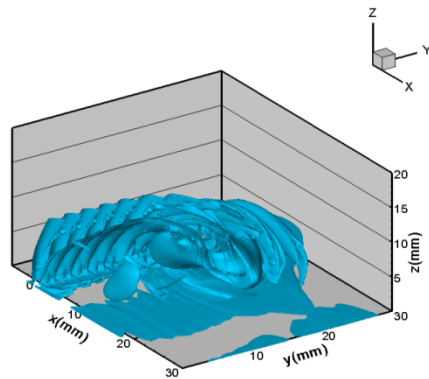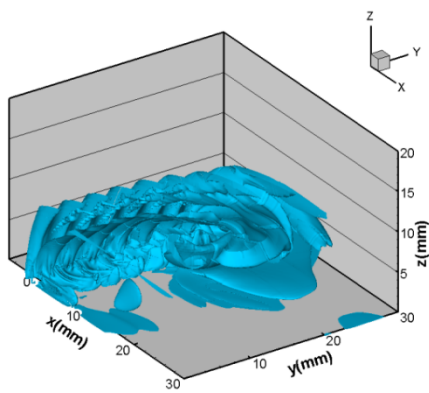
(b) G0.5D1

(c) G1D1
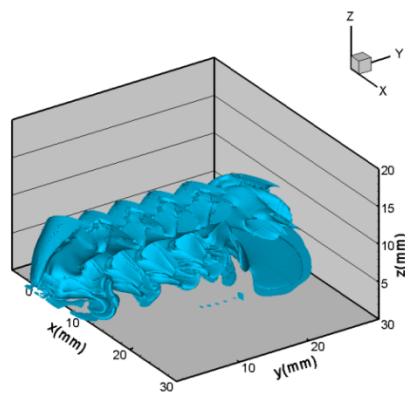
(d) G2D1

Figure 3.14   Close-up view of flow structures at blowing peak
(a) rectangular exit; (b) G0.5D1; (b) G1D1; (c) G2D1
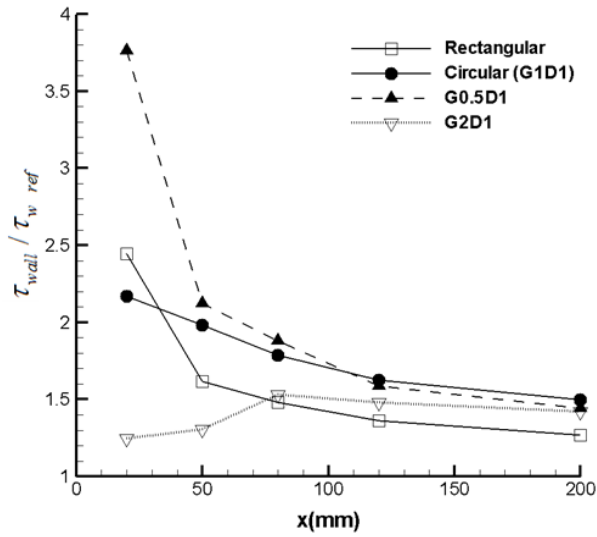
Figure 3.15   Time-averaged streamwise distributions of wall shear stress with variation of the hole gap
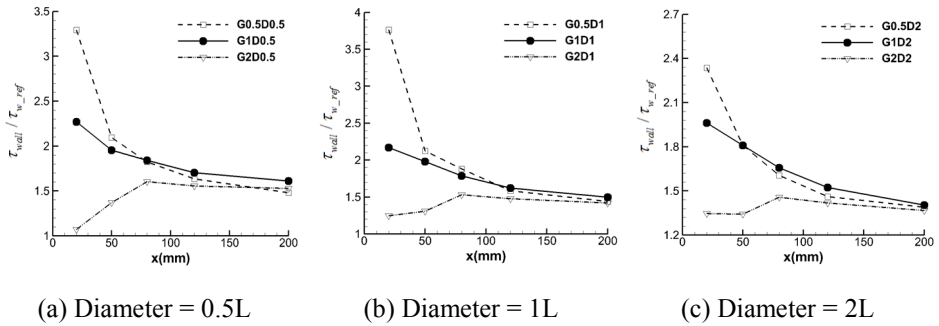
(a) Diameter = 0.5L   (b) Diameter = 1L   (c) Diameter = 2L

Figure 3.16   Time-averaged streamwise distributions of wall shear stress depending on hole gap
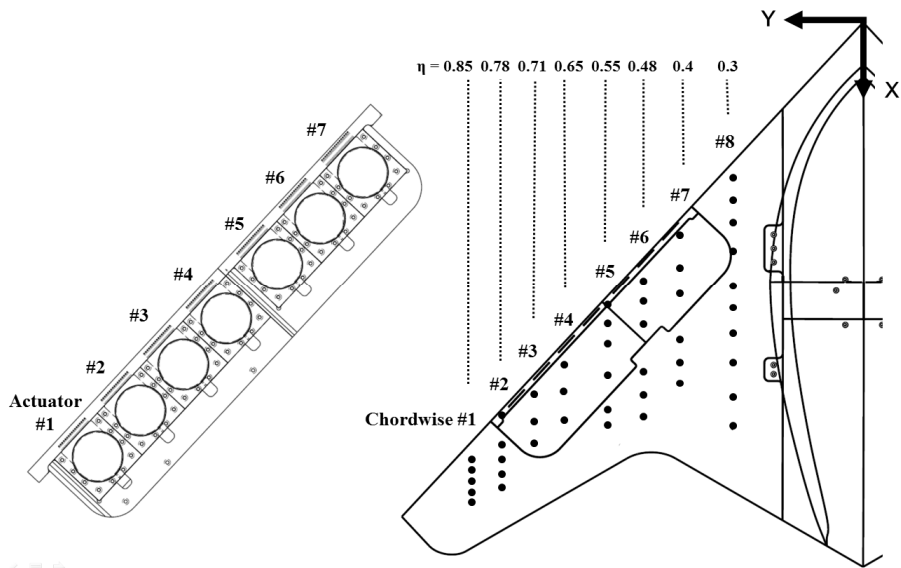
Figure 4.1   BWB model upper surface with synthetic jet and pressure tap
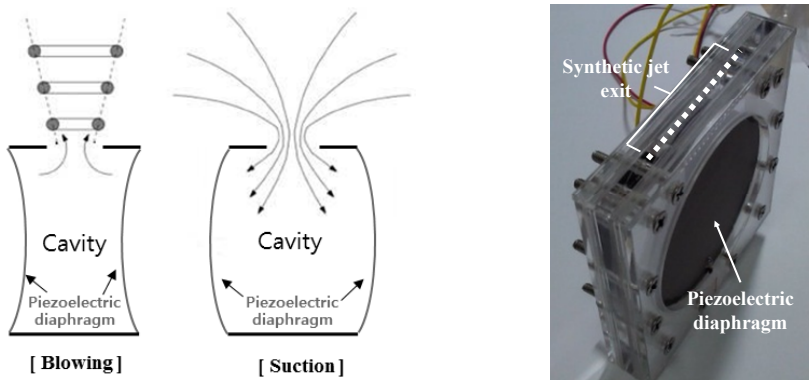
(a) Principle of dual-diaphragm actuator   (b) Manufactured synthetic jet

Figure 4.2   Synthetic jet actuator installed BWB model
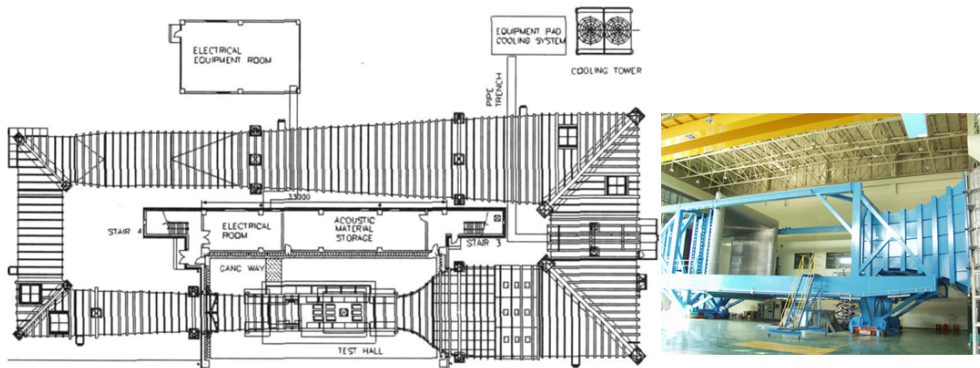
Figure 4.3   Subsonic wind tunnel at KARI
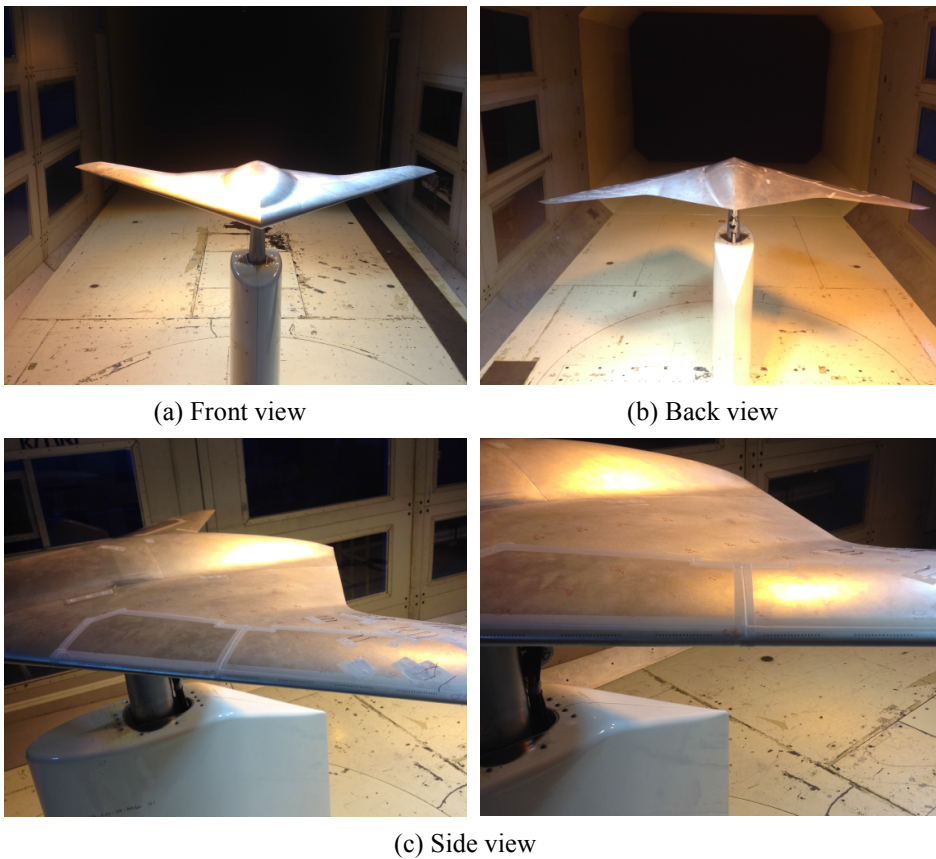
(a) Front view

(b) Back view

(c) Side view

Figure 4.4   BWB wind tunnel model installed in KARI subsonic wind tunnel
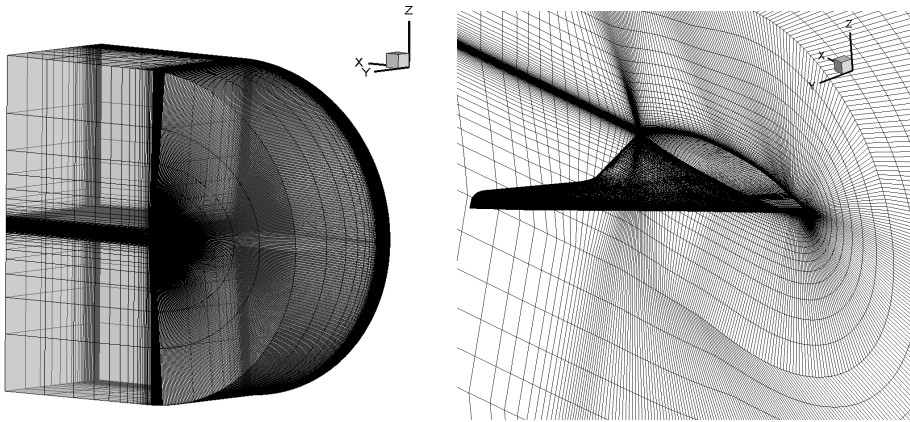
(a) 3-D view of the computational grid   (b) Close-up view of surface grid

Figure 4.5   Computational mesh on BWB configuration
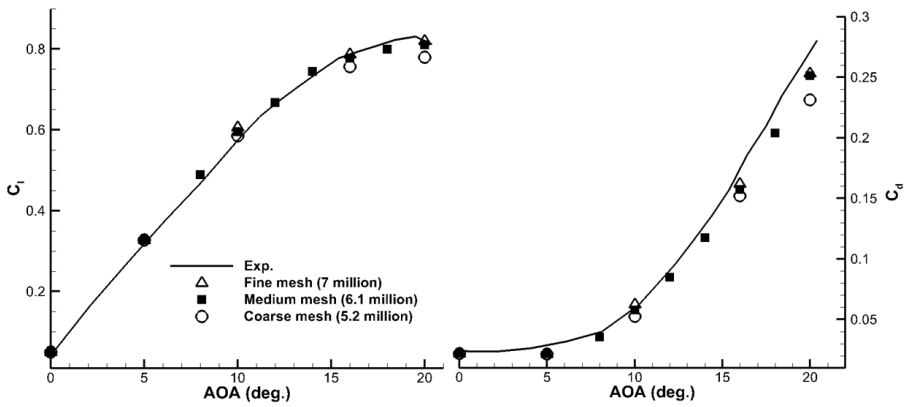
Figure 4.6   Comparison of lift and drag coefficient curves (control-off case)

	Experimental results	Numerical results
(a) AOA = 8 °		
(b) AOA = 10 °		
(c) AOA = 12 °		
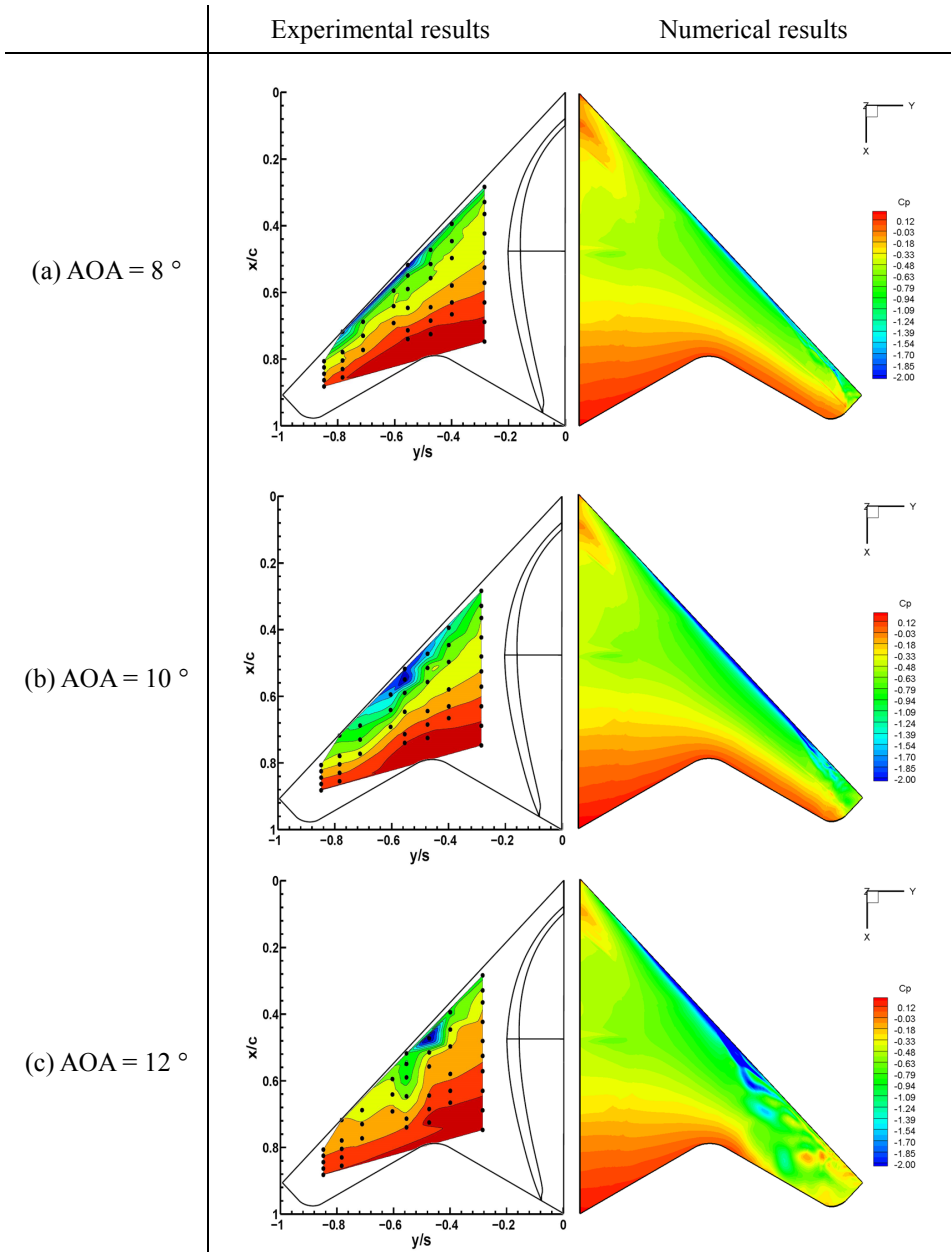
(d) AOA = 14 °
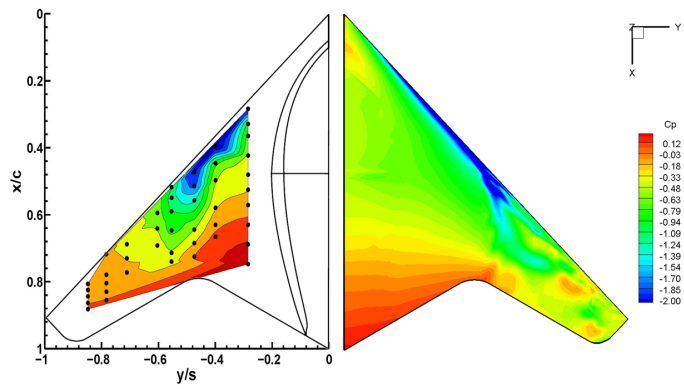
(e) AOA = 16 °
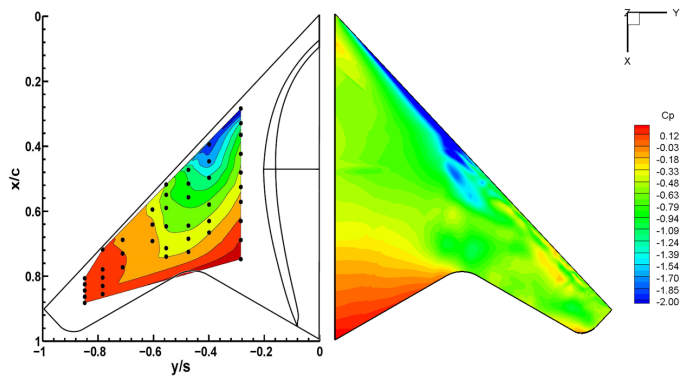
Figure 4.7   Surface pressure coefficient at various angles of attack (control-off case)

(a) AOA = 8 °

(b) AOA = 10 °

(c) AOA = 12 °

(d) AOA = 14 °

(e) AOA = 16 °
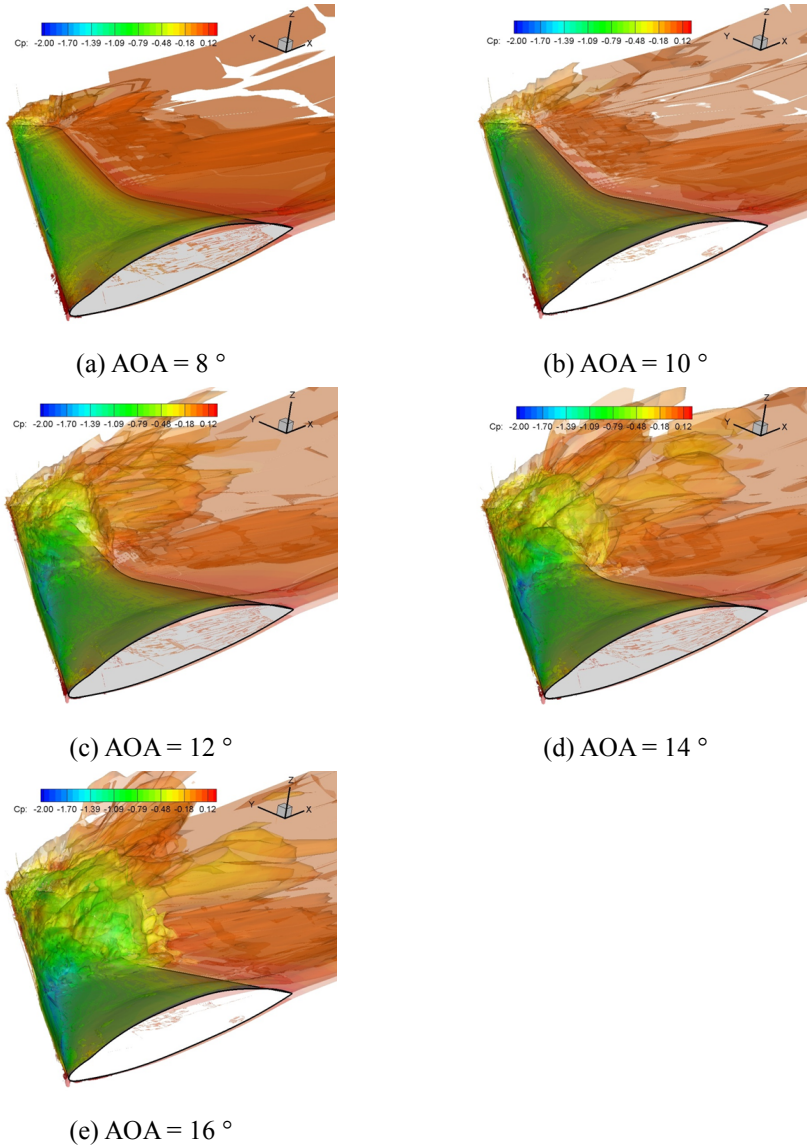
Figure 4.8   Iso-surface vorticity contours at various angles-of-attack

(control-off case)
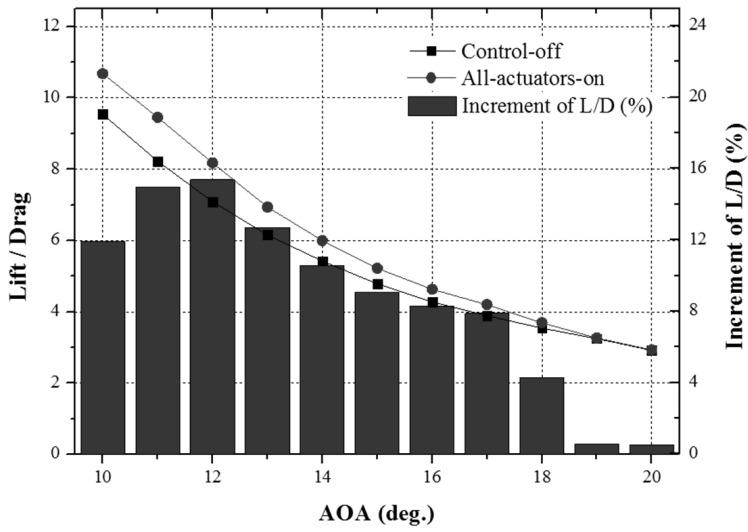
Figure 4.9   Lift to drag curves (all-actuators-on) [66]
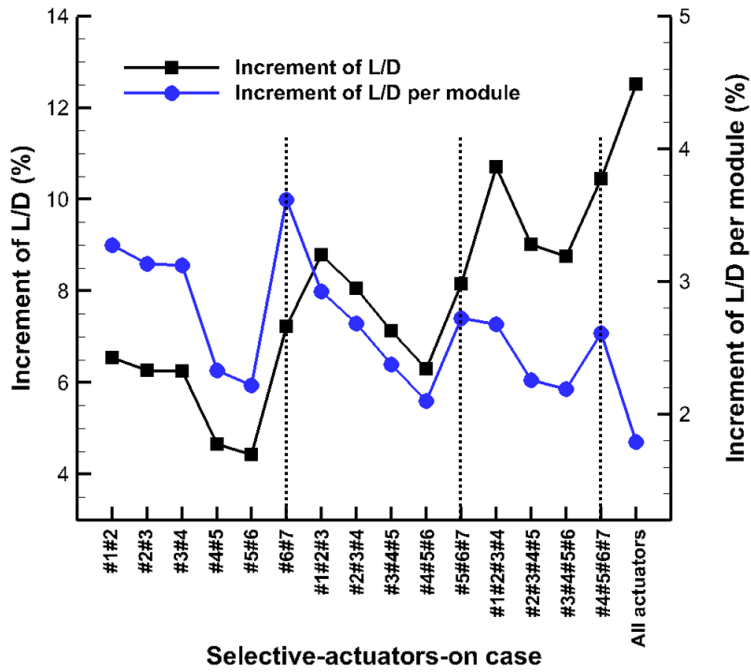
Figure 4.10   Increment of lift to drag (selective-actuators-on) [66]
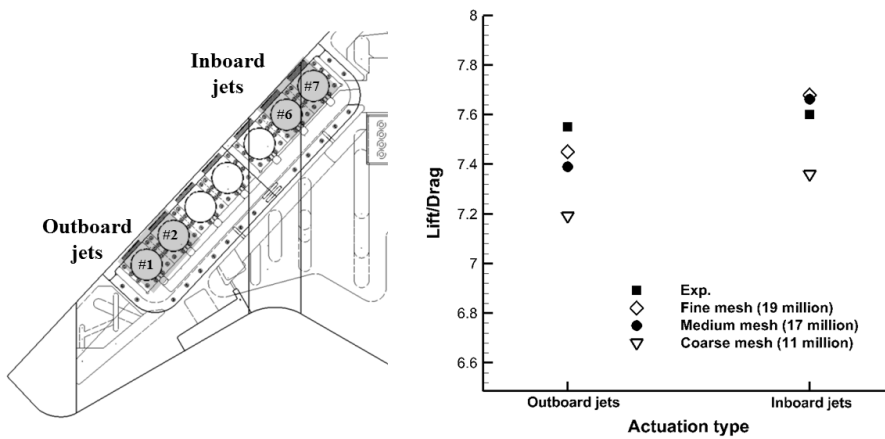
Figure 4.11   Comparison of lift to drag depending on jet location

(a) Inboard jets-on   (b) Outboard jets-on
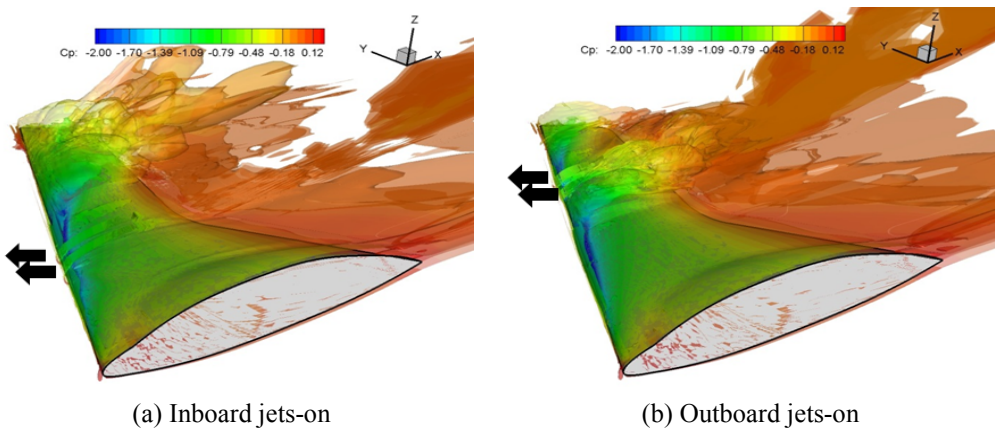
Figure 4.12   Time-averaged iso-surface vorticity contours

depending on jet location
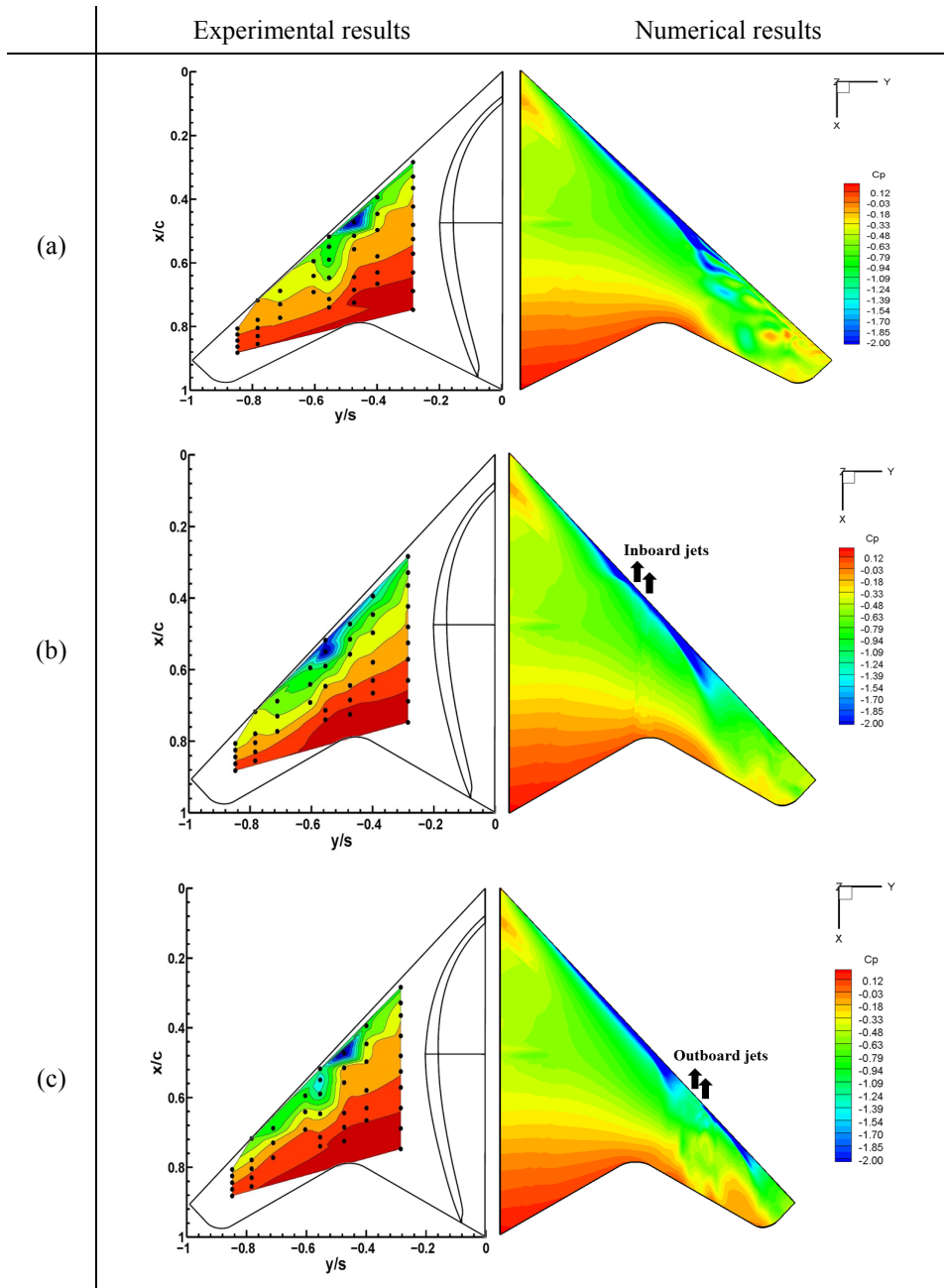
Figure 4.13   Time-averaged surface pressure coefficient according to actuation type (a) control-off; (b) inboard jets-on; (c) outboard jets-on
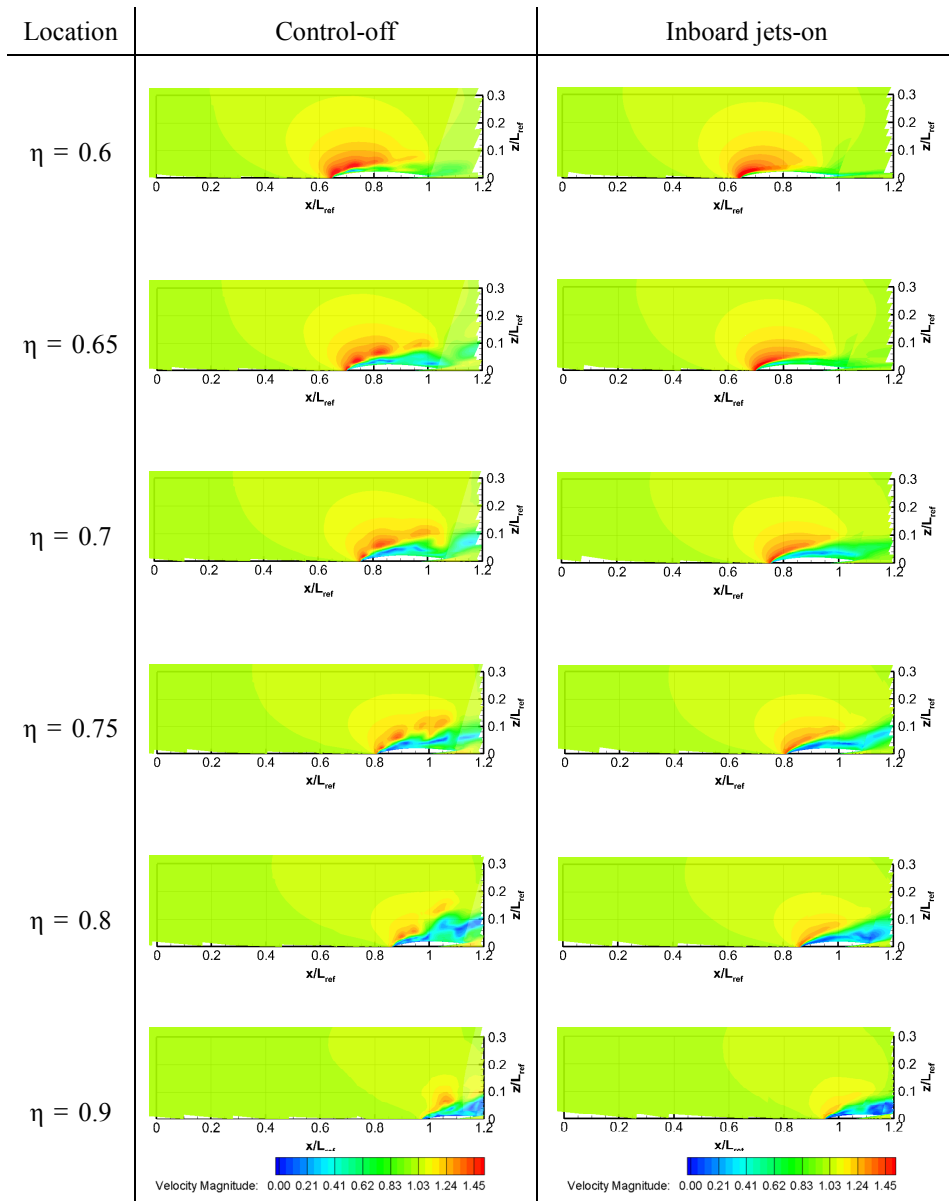
Location	Control-off	Inboard jets-on
η = 0.6		
η = 0.65		
η = 0.7		
η = 0.75		
η = 0.8		
η = 0.9		

Velocity Magnitude: 0.00 0.21 0.41 0.62 0.83 1.03 1.24 1.45

Figure 4.14   Time-averaged pressure coefficient contours at the spanwise plane (inboard jets-on)

Location	Control-off	Outboard jets-on
η = 0.6		
η = 0.7		
η = 0.75		
η = 0.8		
η = 0.85		
η = 0.9		

Velocity Magnitude: 0.00 0.21 0.41 0.62 0.83 1.03 1.24 1.45

Velocity Magnitude: 0.00 0.21 0.41 0.62 0.83 1.03 1.24 1.45
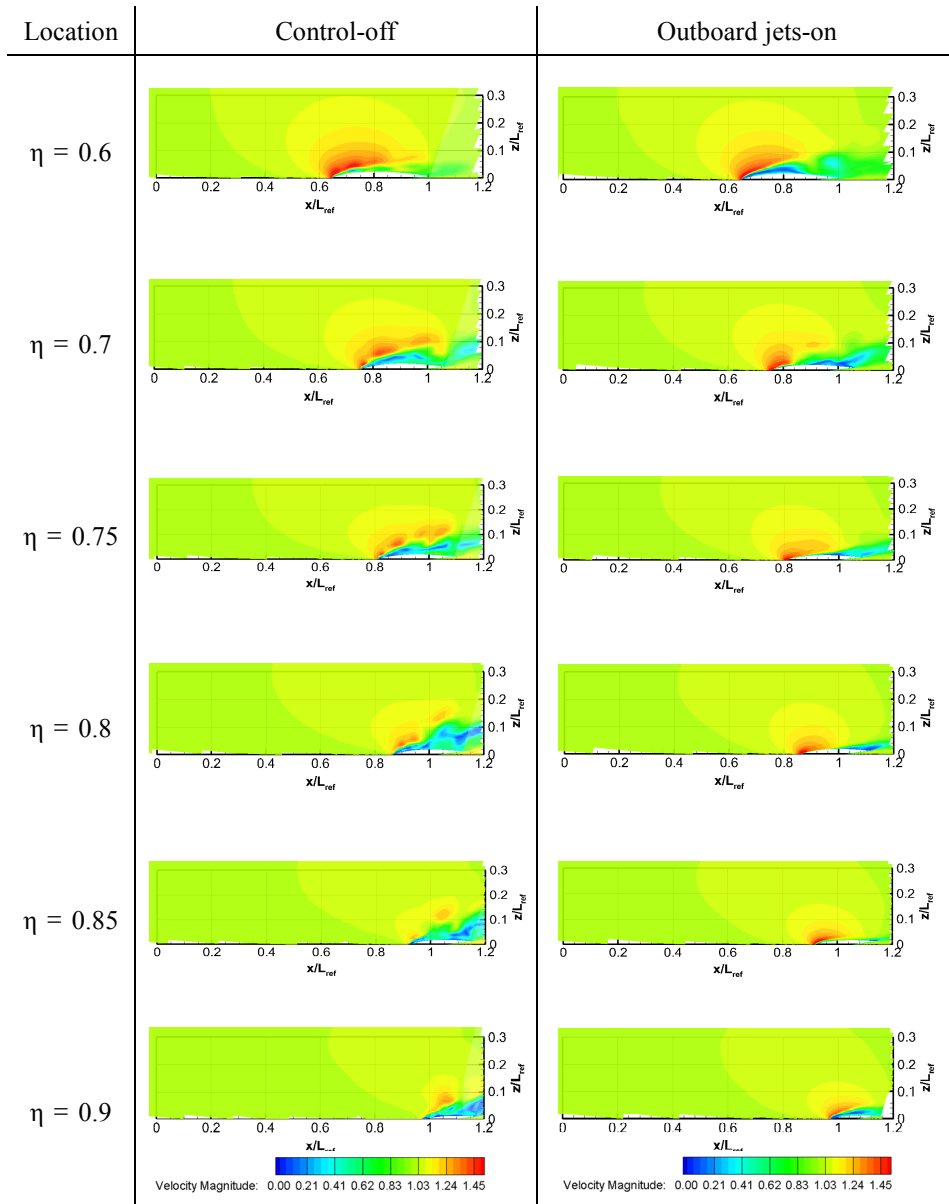
Figure 4.15   Time-averaged pressure coefficient contours at the spanwise plane

(outboard jets-on)
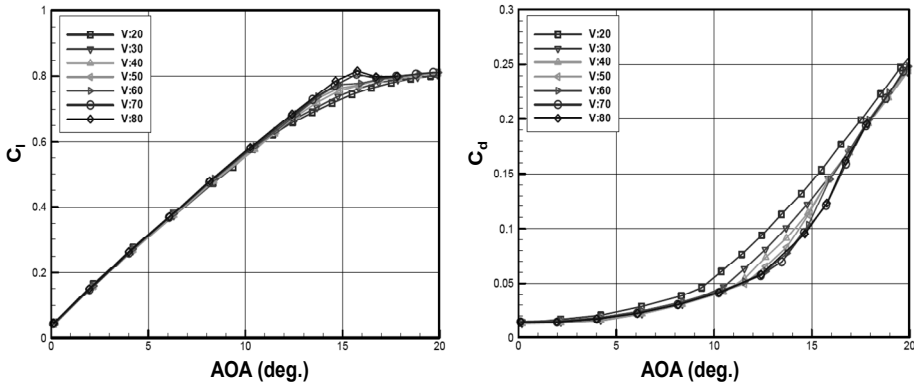
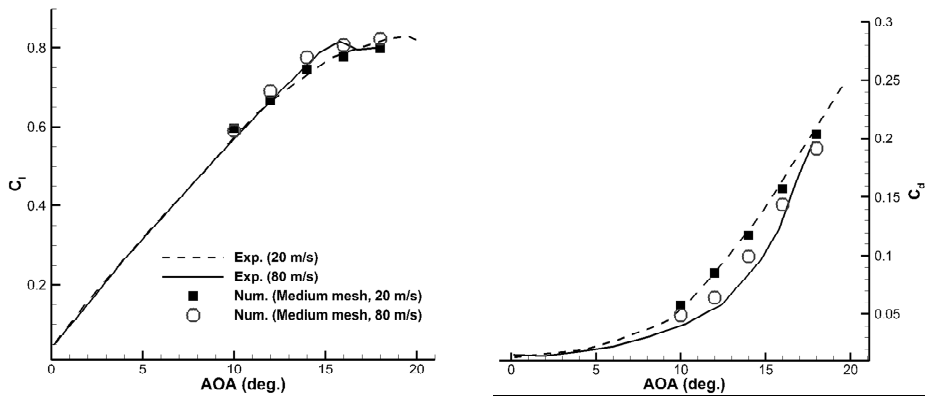**Figure 4.16   Lift to drag curves according to freestream velocity [66]**

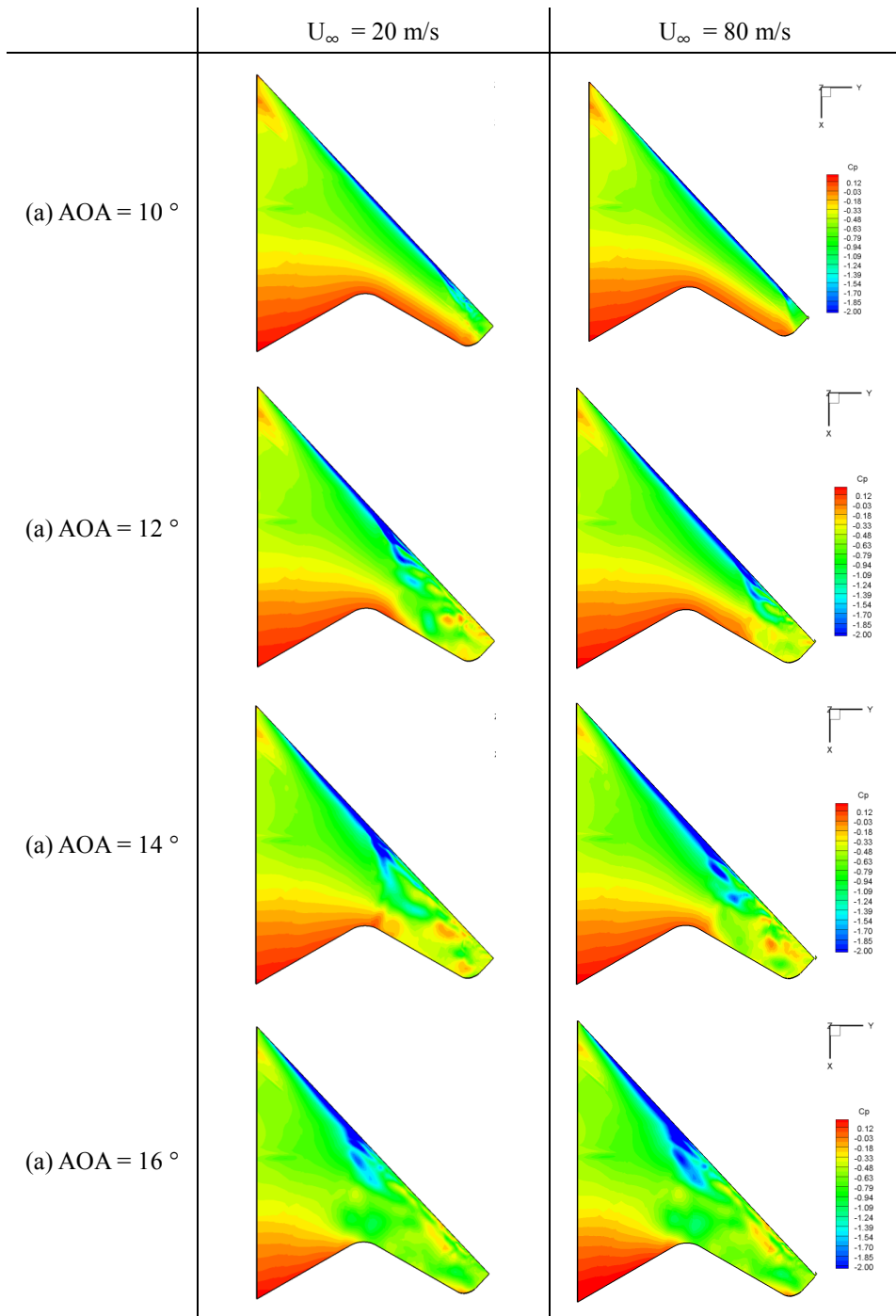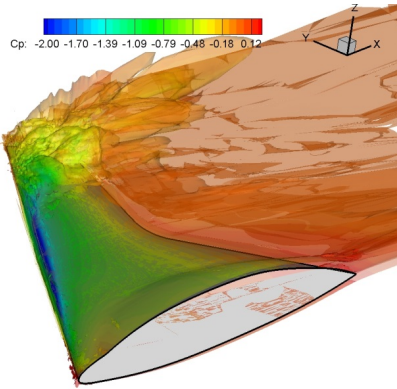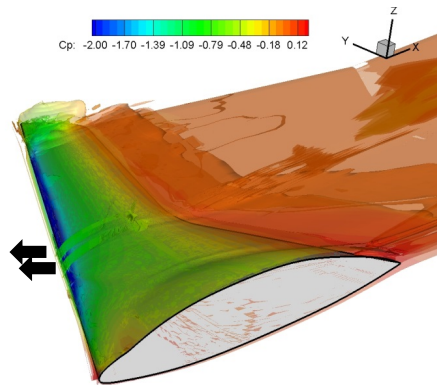**Figure 4.17   Comparison of lift and drag coefficient curves in high speed flight**

	$U_\infty = 20$ m/s	$U_\infty = 80$ m/s
(a) AOA = 10 °		
(a) AOA = 12 °		
(a) AOA = 14 °		
(a) AOA = 16 °		

Figure 4.18   Surface pressure coefficient at U_∞=20 m/s and 80 m/s

(a) Control-off

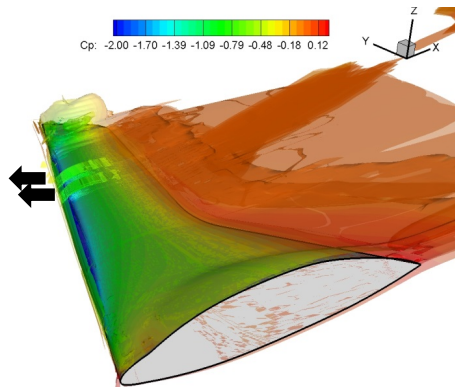(b) Inboard jets-on

(c) Outboard jets-on

Figure 4.19   Time-averaged iso-surface vorticity contours in high speed flight
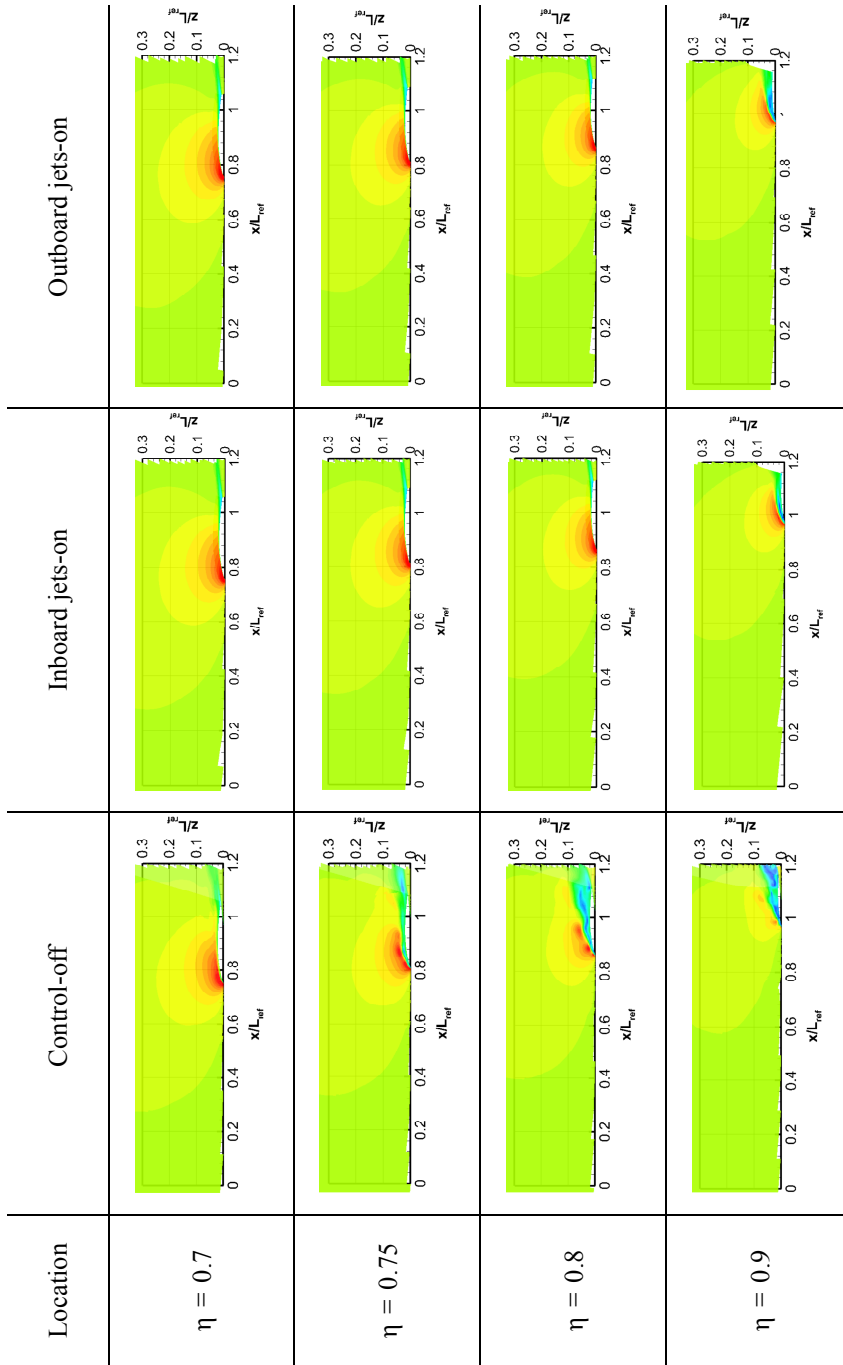
113

Figure 4.20 Time-averaged pressure coefficient contours at the spanwise plane in high speed flight

국문 초록

본 연구는 3차원 날개 형상의 공력 성능을 향상시키기 위하여 synthetic jet을 이용한 공력 특성 향상 메커니즘에 관하여 수치적 연구를 수행하였다. 본 연구를 통하여 synthetic jet의 출구 형상에 따른 유동 특성 파악을 통해 유동제어에 효과적인 출구 형상을 도출하고, 이로부터 얻은 synthetic jet의 형상을 3차원 날개에 적용하여 고 받음각에서의 박리유동 제어 특성을 분석하였다.

Synthetic jet의 출구 형상은 jet vortex의 발달 과정 및 전체적인 jet momentum에 영향을 주기 때문에 유동제어 특성에 큰 영향을 미치는 요인 중 하나이다. 이에 유동제어에 효과적인 출구 형상을 도출하기 위해 평판에서 유입류가 존재할 경우 사각형과 원형 출구 형상에 대하여 jet vortex 유동 구조 및 유동제어 가능성을 분석하였다. 사각형 출구 형상의 경우, jet 출구 직후에서는 큰 와류를 발생시키지만 출구 끝에서 발생하는 회전 유동에 의해 jet에 의한 효과가 급격히 감소함을 확인하였다. 원형 출구 형상의 경우, 사각형 출구 형상보다 균일한 jet vortex를 생성하고 유입류 방향으로 보다 멀리까지 jet의 영향이 미치는 유동구조를 가지고 있어 사각형 출구 형상보다 유동제어에 효과적임을 확인하였다. 또한 원형 출구 형상의 hole gap과 hole diameter의 변화에 따른 유동 구조 및 유동 특성을 비교 분석함으로써 유동제어 효과를 극대화 할 수 있는 원형 출구 형상을 도출하였다.

다양한 수치 해석 결과의 분석을 통해서 도출된 원형 출구 형상의 synthetic jet을 적용하여 동체-날개 혼합 형상의 유동제어를 수행하였다. 풍동 실험과 수치해석을 통해 받음각의 변화에 따른 3차원 날개의 유동 분석을 수행한 결과, 날개의 받음각 증가에 따라 앞전에서부터 발생한 와류유동은 붕괴하게 되며 날개 바깥쪽 부분에서부터는 박리 유동이 발달함을 확인하였다. 이에 와류 붕괴 현상과 박리 유동을 제어하기 위하여 앞전 부근에 jet을 위치시켰다. 풍동 실험을 통하여 앞전에 위치한 jet을 모두 작동 시켜 유동제어 효과를 확인하였다. 또한 고성능, 저전력 구동을 위하여 jet의 개수에 따른 유동제어 성능을 평가하였다. 수치해석을 통하여 jet의 위치에 따른 유동제어 메커니즘을 확인하고 위치에 따라 유동제어를 수행할 경우 와류 붕괴 현상을 지연시키고 박리 유동을 제어할 수 있음을 확인하였다. 또한 고속에서의 유동제어 가능성을 확인하기 위하여 저속에서의 유동제어 전략을 고속에서 확장 적용하여 고속의 동체-날개 혼합형상에서도 효과적인 유동제어 방법을 통하여 고 받음각의 공력 성능을 향상 시킬 수 있음을 확인하였다.

본 연구에서 도출된 연구 결과는 유동제어에 효과적인 능동유동제어 시스템의 설계 및 무인 전투기 형상을 포함한 3차원 날개 형상의 공력 성능 향상 방안 수립에 활용될 수 있을 것이다.

주요어 : 전산유체역학, Synthetic jet, 능동 유동제어, 유동 박리,
　　　　 동체-날개 혼합형상, 와류 구조, 박리 제어
학　　번 : 2010-30129
이　　름 : 김 민 희